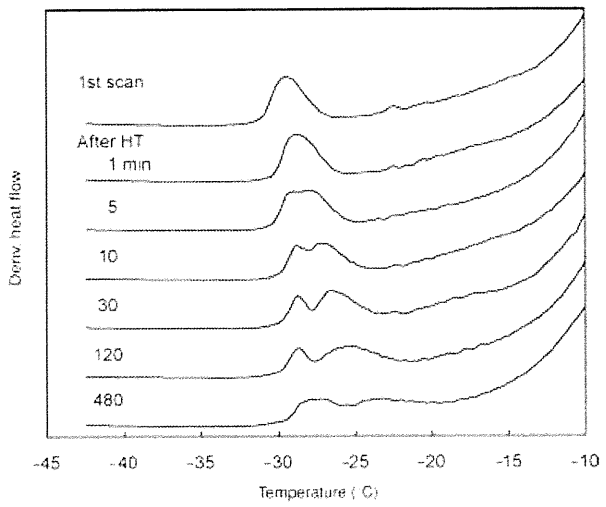

Figure 2. Derivative thermograms of frozen solutions (10 μL) containing 14% sucrose and 6% PVP 29,000 obtained in the first heating scans from −70°C at 5°C/min and in the second scans after heat treatments at −5°C for 1–480 min.

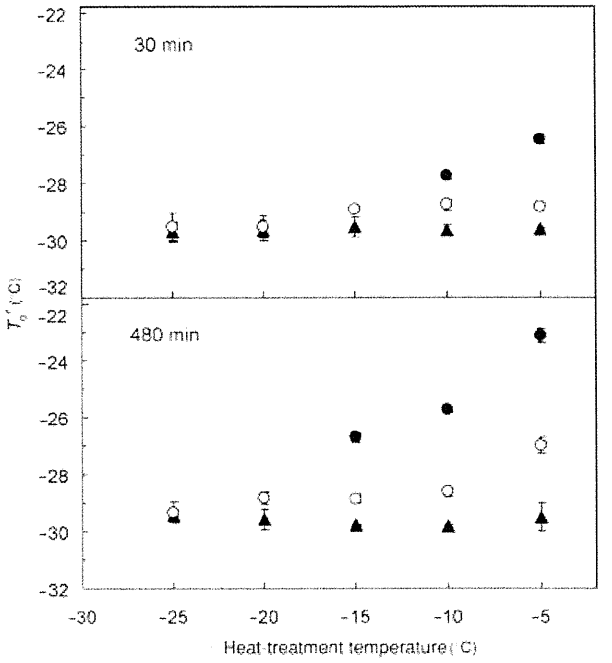

Figure 3. Effects of heat treatment temperatures (−25 to −5°C) on the T_g's of frozen solutions (10 μL) containing 14% sucrose and 6% PVP 29,000 obtained in the scans from −70°C at 5°C/min prior to (▲) and after (○,●) the heat treatment (30, 480 min, $n = 3$, average ± SD).

containing 14% sucrose and 6% PVP 29,000. The heat treatment at higher temperatures (−5°C and −10°C) induced faster splitting of the T_g' peak and an increased margin between the split peaks. Contrarily, the frozen solutions heat treated at lower temperatures (−20°C and −25°C) showed a single transition that was essentially equal to those obtained in the first scan. A longer time was required to induce the apparent T_g' splitting in the heat treatment at the intermediate temperature (−15°C). The heat treatment of the frozen mixture solution at a temperature just below the T_g' (e.g., −35°C, 480 min) resulted in exothermic drift of the thermogram at above the T_g' that suggested the relaxation of the system in the second heating scan (data not shown).[29]

Solutions containing varied total concentrations of sucrose and PVP 29,000 (7:3 weight concentration ratios) were also subjected to thermal analysis in order to study the effect of the heat treatment (Fig. 4). The T_g's obtained in the first scan did not depend largely on the total solute concentrations (5%–20%, w/w). The higher-concentration solutions showed a higher propensity for the T_g' splitting to occur upon the application of the heat treatment at −5°C. The two T_g's that were observed only after the longer heat treatment suggested slower phase separation in the lower-concentration solute mixture solutions (5% total, w/w). This trend was much different from that of the freeze concentration-induced phase separation of polymer mixtures that resulted in two T_g's in the first scan even for lower-concentration solutions.[16]

The frozen solutions containing various saccharides and polymers were subjected to thermal

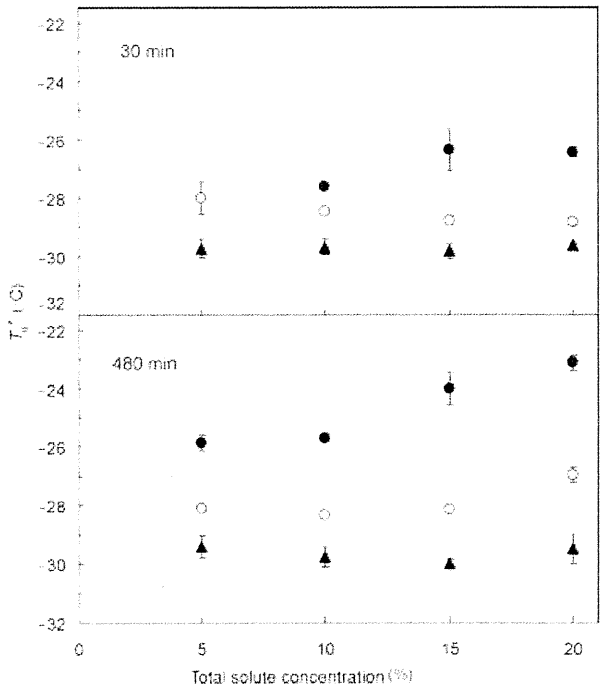

Figure 4. Effects of total solute concentrations on the transition temperatures (T_g's) of frozen solutions (10 μL) containing sucrose and PVP 29,000 at a 7:3 weight ratio scanned from −70°C prior to (▲) and after (○, ●) a heat treatment at −5°C (30, 480 min, $n = 3$, average ± SD).

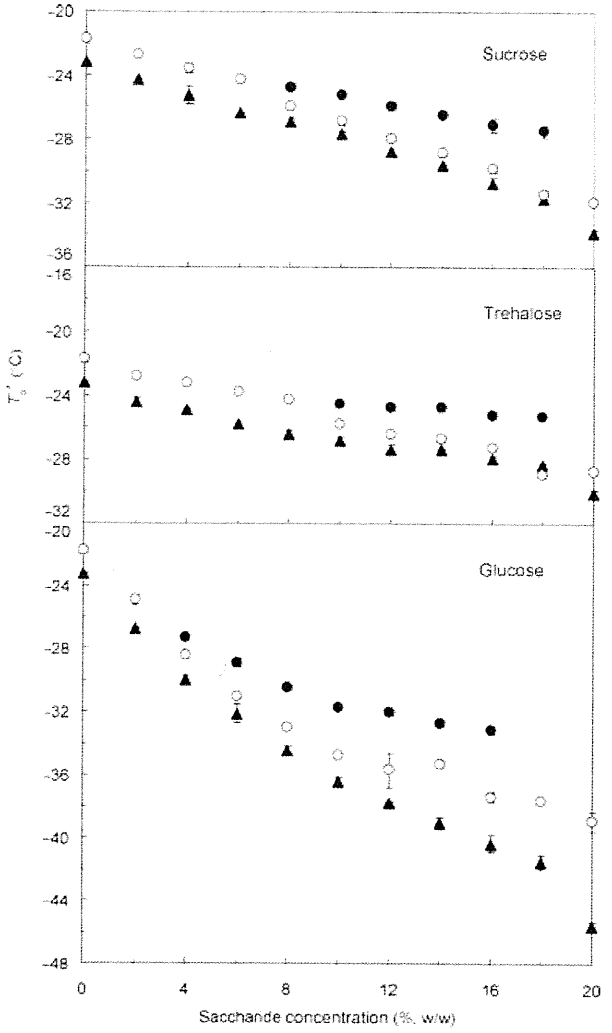

Figure 5. Transition temperatures (T_g's) of frozen solutions (10 μL) containing varied concentration ratios of low-molecular-weight saccharide and PVP 29,000 (total 20%, w/w). Symbols denote T_g's obtained in the heating scans prior to (▲) and after (○, ●) the heat treatment at −5°C for 30 min ($n = 3$, average ± SD).

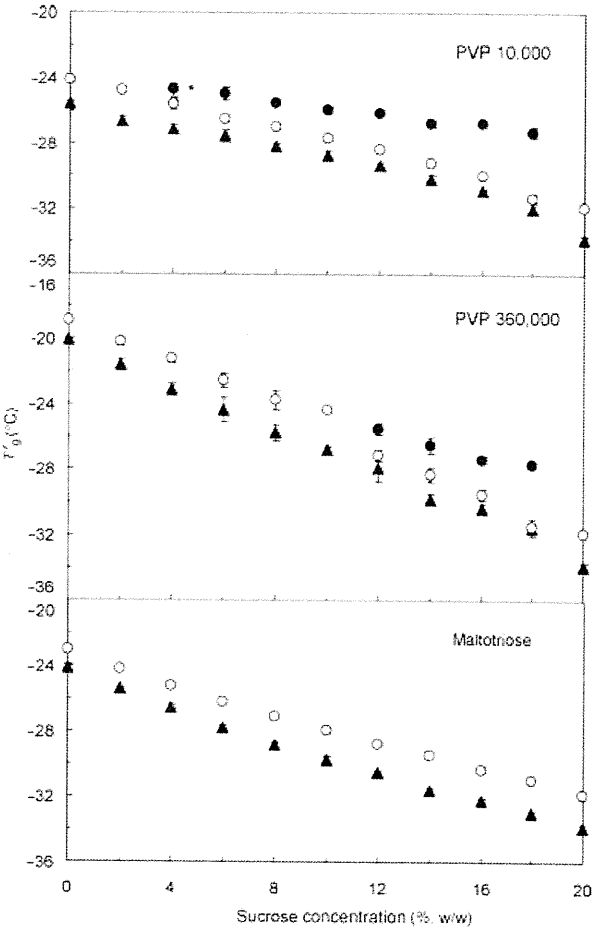

Figure 6. Transition temperatures (T_g's) of frozen solutions (10 μL) containing varied concentration ratios of sucrose and PVP or maltotriose (total 20%, w/w). Symbols denote T_g's obtained in the heating scans prior to (▲) and after (○, ●) the heat treatment at −5°C for 30 min ($n = 3$, average ± SD). *, two transitions were observed in two of three scans.

analysis to elucidate the effect of the heat treatment. The frozen solutions containing saccharide-rich mixtures of PVP 29,000 and disaccharides showed the splitting of the T_g' upon application of the heat treatment (−5°C, 30 min, Fig. 5). Contrarily, the single-solute and polymer-rich frozen solutions showed slight upward shifts of the single T_g's. The heat-treated frozen solutions containing glucose and PVP 29,000 showed two T_g's at wider concentration ratios. The effect of the heat treatment on the transition temperatures of the frozen solutions containing sucrose and varied-molecular-weight PVPs (PVP 10,000, 360,000) is shown in Figure 6. The frozen smaller PVP solution showed the T_g' at lower temperature.[33] The two T_g's were observed at wider concentration ratio in the heat-treated mixtures containing sucrose and smaller PVP molecules (10,000) compared with those containing larger PVP molecules (360,000). The figure also shows the T_g's of the frozen sucrose and maltotriose mixture solutions. The slight upward shift of the single T_g' that occurred upon the application of the heat treatment indicated further concentration of the miscible noncrystalline solutes at all concentration ratios.[34]

The splitting of T_g's should indicate the separation of the freeze-concentrated solutes into multiple phases that differ in their solute compositions upon the application of the heat treatment. This definition of the change, rather than the proposition that a two-step physical property change occurs in a miscible concentrated phase, was better supported by the observation of the T_g' split only in particular frozen solute-mixture solutions. The large effect of the heat treatment temperature and time on the

DOI 10.1002/jps

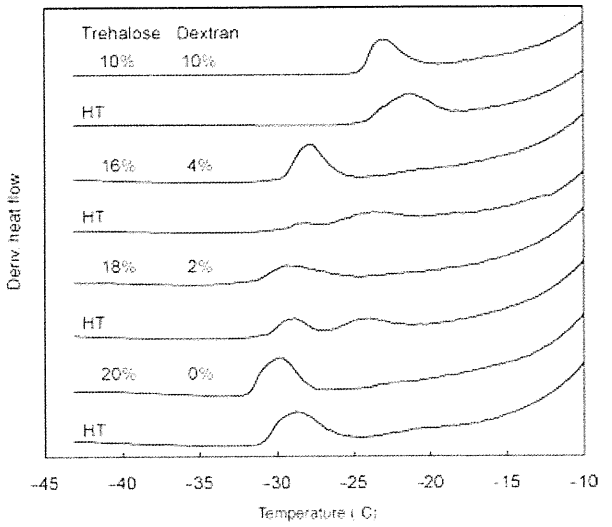

Figure 7. Derivative thermograms of frozen solutions (10 μL) containing varied concentration ratios of trehalose and dextran 40,000 obtained in the heating scans prior to and after the heat treatment at −5°C for 30 min.

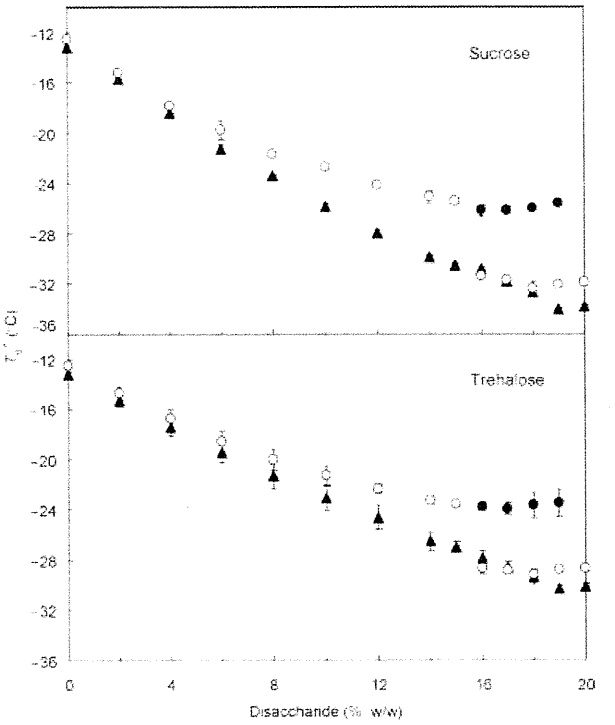

Figure 8. Transition temperatures (T_g's) of frozen solutions (10 μL) containing varied concentration ratios of disaccharide and dextran 40,000 (total 20%, w/w). Symbols denote T_g's obtained in the heating scans prior to (▲) and after (○, ●) the heat treatment at −5°C for 30 min (n = 3, average ± SD).

T_g' splitting strongly suggested that the increasing mobility of water and solute molecules helped to induce the phase separation. Solute compositions in the heat treatment-induced multiple freeze-concentrated phases were not clear from the transition temperatures in the PVP-containing systems.

Heat Treatment of Frozen Disaccharide and Dextran Mixture Solutions

Frozen solutions containing a disaccharide (trehalose and sucrose) and dextran 40,000 also showed a single T_g' in the heating scans prior to the heat treatment (Figure 7 and 8). Exposing the disaccharide-rich frozen mixture solution to a higher temperature (−5°C, 30 min) induced the splitting of the T_g', leading to two peaks in the derivative thermograms. The transition temperature profiles suggested solute compositions in the multiple freeze-concentrated phases of the heat-treated dextran-containing systems. The heat-treated frozen solutions containing 16%–19% trehalose showed their lower temperature transition ($T_g'_{2L}$) near the point of the single transition of the heat-treated frozen trehalose solution, suggesting changes of the concentrated disaccharide phase. The higher temperature transition ($T_g'_{2H}$) phase should contain certain concentration ratios of disaccharide and dextran. Contrarily, the slight upward shift of the single T_g's indicated further concentration of the solute mixture in the heat-treated frozen solutions containing higher concentrations of dextran. The heat treatment induced similar changes in the transition temperatures in the mixtures containing sucrose and dextran 40,000.

The effect of the heat treatment temperatures (−25°C to −5°C) on the T_g' of frozen solutions containing 18% trehalose and 2% dextran 40,000 is shown in Figure 9. Exposing the frozen solutions to higher temperatures (−5°C and −10°C) induced faster splitting of the T_g's. The frozen solution maintained a single T_g' upon the application of the heat treatment at a temperature just above T_g' (−25°C). The longer heat treatment (480 min) at the intermediate temperatures induced T_g' splitting (−20°C) or increased the margin between the two T_g' peaks (−15°C and −10°C). This result also indicates that higher solute mobility contributed to the phase separation of the multisolute frozen solutions. No changes that suggest the crystallization of trehalose were observed in these frozen mixture solutions.[35]

Some frozen solutions containing sucrose and a polymer were freeze-dried in the DSC cells with or without prior heat treatment at −5°C (60 min) to study the physical properties of the resulting solids. The heating scan of the sucrose solid that was freeze-dried without the heat treatment showed glass transition (T_g: 70.2°C), sucrose crystallization exotherm (onset at ~120°C), and sucrose crystal melting endotherm (~180°C, Fig. 10, some data not shown). Colyophilization with dextran 40,000 or PVP

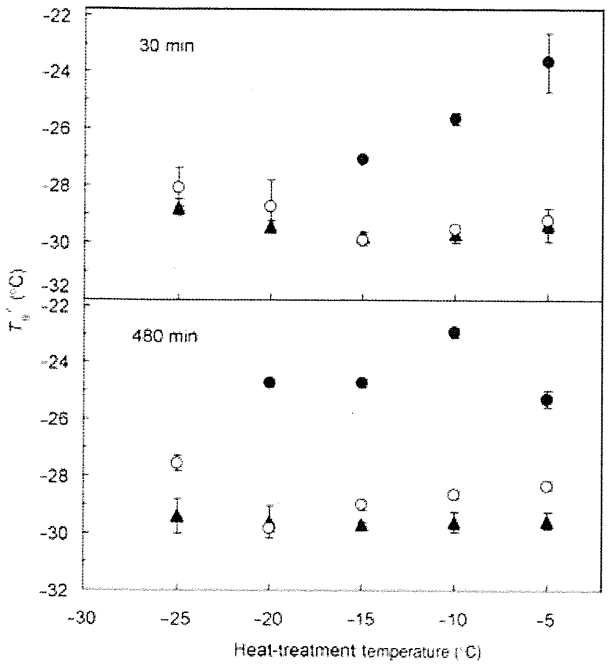

Figure 9. Effect of heat treatment temperatures (−25°C to −5°C) on the T_g' of frozen solutions (10 μL) containing 18% sucrose and 2% dextran 40,000 obtained by the heating scan (5°C/min) from −70°C prior to (▲) and after (○, ●) the heat treatment (30, 480 min, $n = 3$, average ± SD).

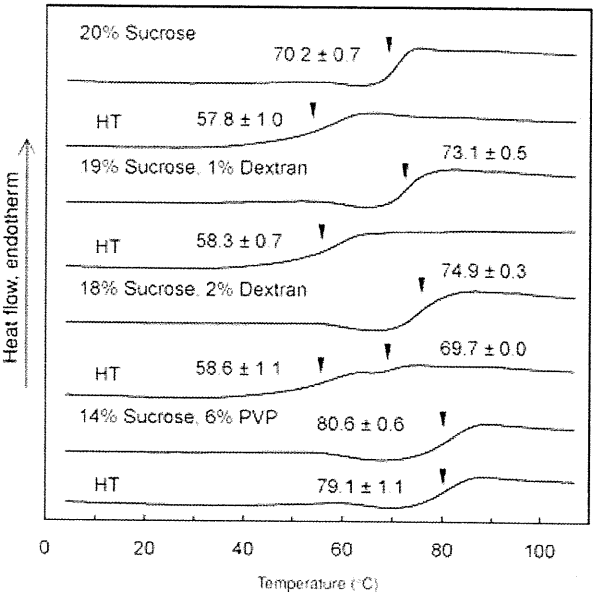

Figure 10. Thermograms of disaccharide-and-polymer mixture solids freeze-dried with and without prior heat treatment at −5°C for 60 min. The solids (~2 mg) in aluminum cells were scanned from −20°C at the heating rate of 5°C/min. The numbers denote average glass transition temperature ± SD ($n = 3$).

29,000 raised the T_gs of the dried sucrose solids to some extent. The heat treatment did not significantly alter the overall appearance of the microporous cake solids dried in glass vials. Some solids showed apparent changes of their thermal properties due to the heat treatment. The heat treatment of frozen solutions broadened and lowered the glass transition of the subsequently freeze-dried sucrose or sucrose and dextran mixture solids. The heat treatment of frozen 18% sucrose and 2% dextran mixture solution induced apparent two-step heat capacity changes of the dried solids, suggesting glass transitions of the separated phases. Reasons of the broader transitions in other heat-treated solids were not clear. The prior heat treatment did not alter the glass transition of solids lyophilized from solutions containing 14% sucrose and 6% PVP 29,000.

Possible Physical Changes Induced by the Heat Treatment

The nature of the observed physical changes and their effects on the quality of pharmaceutical formulations are of particular interest. The thermal profiles strongly suggested different underlying mechanisms that induced the multiple freeze-concentrated phases between the solutions containing certain multiple polymers and the disaccharide and polymer mixtures. Increasing concentration during ice growth and their thermodynamic incompatibility are considered as major causes of the phase separation upon freezing of some dilute single-phase multipolymer solutions.[14,16,17] The heat treatment has smaller effect to alter miscibility of the PVP and dextran in the frozen solutions.[16]

Freezing of many other aqueous solutions concentrates the multiple solutes into a single mixture noncrystalline phase, showing the single T_g's because the mixing is thermodynamically favorable or because the increasing viscosity at the higher concentrations and low temperatures, particularly below the T_g's, kinetically prevent the solute phase separation. The increasing solute mobility accompanying the viscosity drop during the heat treatment of the frozen solutions should allow spatial rearrangement of the kinetically trapped molecules into the thermodynamically favorable multiple phases that differ in their compositions. Reported phase separation of some lyophilized disaccharide and dextran mixtures upon exposure to the higher humidity and temperature indicate limitations in the miscibility of the noncrystalline molecules.[28] It is plausible that the mixing of disaccharide and dextran in the freeze-concentrated solutions and in the highly humidified solids depend on the same "solid solubility" factors.[28,36,37] It is widely accepted that the mobility of the noncrystalline solute and hydrating water molecules significantly increase at temperatures above T_g', although there have been long debates on the definition and naming of the thermal transitions that appear in thermal analysis.[31,32]

DOI 10.1002/jps

The apparent effect of the heat treatment temperature and time clearly indicated contribution of the increasing solute mobility on the phase separation. Wide ranges of pharmaceutically relevant solute mixtures should be susceptible to this type of miscibility change. The additional ice crystallization occurs during the heat treatment or the following cooling process should raise the T_g' obtained in the second heating scans.

The varied transition temperature profiles suggested different mixing behaviors of the disaccharides and polymers in the heat-treated frozen solutions. The frozen solutions containing a disaccharide and dextran 40,000 suggested separation of the solutes into a disaccharide-dominant $T_g'_{2L}$ phase and a solute-mixture $T_g'_{2H}$ phase upon the application of the heat treatment. The transition temperatures of the concentrated solute mixture phase ($T_g'_{2H}$) (sucrose and dextran 40,000: approximately −26°C; trehalose and dextran 40,000: approximately −23°C) suggested mixing of the disaccharide and dextran at approximately 2–3:1 weight concentration ratios. The surplus disaccharide molecules above these concentration ratios would be removed from the mixture to form the disaccharide-dominant concentrated phase upon the application of the heat treatment presumably because the interactions (e.g., hydrogen bonding) between the same molecules were thermodynamically more favorable than those between heterogeneous components. The separation into disaccharide-dominant and solute-mixture phases is consistent with the reported phase separation of a humidified freeze-dried trehalose and dextran mixture, which leads to trehalose crystallization.[28] The complex T_g' profiles of the heat-treated disaccharide and PVP mixture frozen solutions suggested that the differences in the solute compositions between the two freeze-concentrated phases were smaller than that of the disaccharide and dextran mixture. The expected higher mobility of smaller PVP molecules at the heat treatment temperature would explain the T_g' splitting observed at wider concentration ratios. The solute miscibility information revealed by the thermal analysis has some limitations because at least a certain fraction of the components should be phase separated to show the transition detectable by DSC.[21] The reason the total solute concentration affected the occurrence of the phase separation remains unclear.

In addition to the heat treatment process, some multisolute frozen solutions would unintentionally experience the high solute mobility temperatures that allow the solute phase separation during the freezing process of lyophilization. The freezing of larger volume solutions in glass vials often keeps them at temperatures close to 0°C for a certain period during the ice growth because of the large enthalpy of ice fusion, limited heat flow through the vial bottoms, and slow shelf-cooling speed. The possible intervial and interbatch variations of the thermal history would affect the morphology of the ice crystals as well as the miscibility of the noncrystalline solutes. Contrarily, the small amounts of solutions in aluminum DSC cells, which are designed to constantly follow the stage temperatures, should provide a limited time for the solute phase separation to occur during the cooling process of the thermal analysis. The observed slow phase separation during the heat treatment at a relatively low temperature (−20°C) also suggested the occurrence of this phenomena during practical freeze-drying processes. Some "controlled ice nucleation" techniques are getting increasing attention as ways to achieve uniform ice structure and sublimation speed among vials.[38] Inducing the simultaneous freezing of solutions in many vials before the spontaneous freezing can keep them at temperatures well above the T_g' longer than the usual freezing processes.

Implications for Freeze-Dried Formulation Quality

The phase separation of the freeze-concentrated solutes induced by the heat treatment should directly and/or indirectly affect the quality of various freeze-dried pharmaceutical formulations. The ability of disaccharides to protect higher-order structure of the therapeutic proteins and liposomes against the dehydration stresses depends on the number and strength of the water-substituting molecular interactions in the glass-state mixtures.[4,5] The disaccharide and polymer mixtures studied did not show the miscibility change that apparently decreases the hetero-solute interactions. However, possible separation into the phases both dominant in one of the solutes, as observed in the freeze-concentration-induced separation of multiple polymers, should lead to loss of the stabilizing interactions.

Different transition temperatures of the individual phases should provide chances for physical and chemical changes of the formulation properties during the process and storage. The possible higher molecular mobility in the lower glass transition temperature solid phase would allow chemical degradation of the ingredients during the storage. Varied distribution of other solutes (e.g., inorganic salts) into the multiple concentrated phases should further affect stability of APIs that depends largely on the local environment (e.g., T_g and pH). The multiple concentrated phases in a frozen solution may have independent propensities toward physical collapse during the primary drying. Primary drying of some phase-separating polymer mixtures at the product temperatures between the collapse temperatures (T_cs) of the consisting noncrystalline concentrated phases results in microcollapsed cakes composed of a skeletal ordered higher T_c phase and a structurally disordered phase.[39]

The heat treatment of frozen solutions may also affect quality of the lyophilized formulations even without the phase separation. The ice crystal size growth resulting from the heat treatment of frozen solutions allows faster ice sublimation, whereas the accompanying reduction of the specific surface area of the solid matrix should increase the time required for the secondary drying segment.[2] The reordering of the miscible solute molecules by the heat treatment of the frozen solutions as well as the relaxation of the freeze-concentrated solutes during the storage at the temperature just below T_g' are possible factors that alter the physical property of dried solids. Further characterization of the solids is clearly needed to elucidate the implications of these changes.[40,41]

These findings suggested some strategies to improve the quality of freeze-dried pharmaceuticals through controlling the component miscibilities. For example, the transition temperature profile helps in the setting of appropriate ingredient compositions that avoid component phase separation during the freeze-drying process. Intentionally inducing the phase separation by the heat treatment would be an alternative way to reduce the variations of the physical properties in certain formulations. The fact that the component immiscibility can affect the formulation qualities highlights the relevance of appropriate formulation design and process control based on the quality by design concept because it is not easy to visually discriminate the dried cakes that have been unintentionally separated into multiple phases during the process. Further studies using other mixture systems and analytical methods (e.g., temperature-modulated DSC, Raman imaging, and NIR imaging) would provide deeper insight into the T_g' splitting physical changes and their effects on the formulation quality. It is of particular interest how the heat treatment of frozen solutions affects the quality of lyophilized therapeutic protein and drug delivery system formulations.

ACKNOWLEDGMENTS

This study was partially supported by the Japan Human Sciences Foundation (KHB 1005).

REFERENCES

1. Manning MC, Chou DK, Murphy BM, Payne RW, Katayama DS. 2010. Stability of protein pharmaceuticals: An update. Pharm Res 27:544–575.
2. Wang W. 2000. Lyophilization and development of solid protein pharmaceuticals. Int J Pharm 203(1–2):1–60.
3. Chen C, Han D, Cai C, Tang X. 2010. An overview of liposome lyophilization and its future potential. J Control Release 142:299–311.
4. Bhatnagar BS, Bogner RH, Pikal MJ. 2007. Protein stability during freezing: Separation of stresses and mechanisms of protein stabilization. Pharm Dev Technol 12(5):505–523.
5. Carpenter JF, Chang BS, Garzon-Rodriguez W, Randolph TW. 2002. Rational design of stable lyophilized protein formulations: Theory and practice. Pharm Biotechnol 13:109–133.
6. Jovanović N, Gerich A, Bouchard A, Jiskoot W. 2006. Near-infrared imaging for studying homogeneity of protein–sugar mixtures. Pharm Res 23(9):2002–2013.
7. Katayama DS, Carpenter JF, Menard KP, Manning MC, Randolph TW. 2009. Mixing properties of lyophilized protein systems: A spectroscopic and calorimetric study. J Pharm Sci 98(9):2954–2969.
8. Padilla AM, Pikal MJ. 2011. The study of phase separation in amorphous freeze-dried systems, part 2: Investigation of Raman mapping as a tool for studying amorphous phase separation in freeze-dried protein formulations. J Pharm Sci 100
9. Shamblin SL, Taylor LS, Zografi G. 1998. Mixing behavior of colyophilized binary systems. J Pharm Sci 87:694–701.
10. Taylor LS, Zografi G. 1998. Sugar-polymer hydrogen bond interactions in lyophilized amorphous mixtures. J Pharm Sci 87(12):1615–1621.
11. Newman A, Engers D, Bates S, Ivanisevic I, Kelly RC, Zografi G. 2008. Characterization of amorphous API: Polymer mixtures using X-ray powder diffraction. J Pharm Sci 97:4840–4856.
12. MacKenzie AP. 1977. The physico-chemical basis for the freeze-drying process. Develop Biol Stand 36:51–67.
13. Nail SL, Jiang S, Chongprasert S, Knopp SA. 2002. Fundamentals of freeze-drying. Pharm Biotechnol 14:281–360.
14. Heller MC, Carpenter JF, Randolph TW. 1996. Effects of phase separating systems on lyophilized hemoglobin. J Pharm Sci 85(12):1358–1362.
15. Heller MC, Carpenter JF, Randolph TW. 1999. Application of a thermodynamic model to the prediction of phase separations in freeze-concentrated formulations for protein lyophilization. Arch Biochem Biophys 363:191–201.
16. Izutsu K, Aoyagi N, Kojima S. 2005. Effect of polymer size and cosolutes on phase separation of poly(vinylpyrrolidone) (PVP) and dextran in frozen solutions. J Pharm Sci 94(4):709–717.
17. Randolph TW. 1997. Phase separation of excipients during lyophilization: Effects on protein stability. J Pharm Sci 86(11):1198–1203.
18. Her LM, Deras M, Nail SL. 1995. Electrolyte-induced changes in glass transition temperatures of freeze-concentrated solutes. Pharm Res 12(5):768–772.
19. Zaslavsky BY. 1995. Aqueous two-phase partitioning. New York: Marcel Dekker.
20. Izutsu K, Heller M, Randolph TW, Carpenter JF. 1998. Effect of salts and sugars on phase separation of polyvinylpyrrolidone-dextran solutions induced by freeze-concentration. J Chem Soc Faraday Trans 94:411–418.
21. Padilla AM, Ivanisevic I, Yang Y, Engers D, Bogner RH, Pikal MJ. 2011. The study of phase separation in amorphous freeze-dried systems. Part I: Raman mapping and computational analysis of XRPD data in model polymer systems. J Pharm Sci 100:206–222.
22. Izutsu K, Yoshioka S, Kojima S, Randolph TW, Carpenter JF. 1996. Effects of sugars and polymers on crystallization of poly(ethylene glycol) in frozen solutions: Phase separation between incompatible polymers. Pharm Res 13:1393–1400.
23. Akers MJ, Vasudevan V, Stickelmeyer M. 2002. Formulation development of protein dosage forms. Pharm Biotechnol 14:47–127.
24. Pyne A, Suryanarayanan R. 2003. The effect of additives on the crystallization of cefazolin sodium during freeze-drying. Pharm Res 20:283–291.
25. Searles JA, Carpenter JF, Randolph TW. 2001. Annealing to optimize the primary drying rate, reduce freezing-induced

drying rate heterogeneity, and determine T'(g) in pharmaceutical lyophilization. J Pharm Sci 90(7):872–887.
26. Murase N, Franks F. 1989. Salt precipitation during the freeze-concentration of phosphate buffer solutions. Biophys Chem 34:293–300.
27. Varshney DB, Kumar S, Shalaev EY, Kang SW, Gatlin LA, Suryanarayanan R. 2006. Solute crystallization in frozen systems—Use of synchrotron radiation to improve sensitivity. Pharm Res 23:2368–2374.
28. Vasanthavada M, Tong WQ, Joshi Y, Kislalioglu MS. 2004. Phase behavior of amorphous molecular dispersions I: Determination of the degree and mechanism of solid solubility. Pharm Res 21:1598–1606.
29. Ekdawi-Sever N, Goentoro LA, De Pablo JJ. 2006. Effects of annealing on freeze-dried *Lactobacillus acidophilus*. J Food Sci 68:2504–2511.
30. Luthra SA, Hodge IM, Pikal MJ. 2008. Investigation of the impact of annealing on global molecular mobility in glasses: Optimization for stabilization of amorphous pharmaceuticals. J Pharm Sci 97:3865–3882.
31. Sacha GA, Nail SL. 2009. Thermal analysis of frozen solutions: Multiple glass transitions in amorphous systems. J Pharm Sci 98(9):3397–3405.
32. Wu J, Reading M, Craig DQ. 2008. Application of calorimetry, sub-ambient atomic force microscopy and dynamic mechanical analysis to the study of frozen aqueous trehalose solutions. Pharm Res 25:1396–1404.
33. Levine H, Slade L. 1988. Thermomechanical properties of small-carbohydrate-water glasses and 'rubbers'. J Chem Soc Faraday Trans 1 84:2619–2633.
34. Orford PD, Parker R, Ring SG. 1990. Aspects of the glass transition behaviour of mixtures of carbohydrates of low molecular weight Carbohydr Res 196:11–18.
35. Sundaramurthi P, Patapoff TW, Suryanarayanan R. 2010. Crystallization of trehalose in frozen solutions and its phase behavior during drying. Pharm Res 27(11):2374–2383.
36. Panyam J, Williams D, Dash A, Leslie-Pelecky D, Labhasetwar V. 2004. Solid-state solubility influences encapsulation and release of hydrophobic drugs from PLGA/PLA nanoparticles. J Pharm Sci 93:1804–1814.
37. Vasanthavada M, Tong WQ, Joshi Y, Kislalioglu MS. 2005. Phase behavior of amorphous molecular dispersions II: Role of hydrogen bonding in solid solubility and phase separation kinetics. Pharm Res 22:440–448.
38. Patel SM, Bhugra C, Pikal MJ. 2009. Reduced pressure ice fog technique for controlled ice nucleation during freeze-drying. AAPS PharmSciTech 10(4):1406–1411.
39. Izutsu K, Fujii K, Katori C, Yomota C, Kawanishi T, Yoshihashi Y, Yonemochi E, Terada K. 2010. Effects of solute miscibility on the micro- and macroscopic structural integrity of freeze-dried solids. J Pharm Sci 99(11):4710–4719.
40. Townrow S, Roussenova M, Giardiello M-I, Alam A, Ubbink J. 2010. Specific volume–hole volume correlations in amorphous carbohydrates: Effect of temperature, molecular weight, and water content. J Phys Chem B 114:1568–1578.
41. Imamura K, Asano Y, Maruyama Y, Yokoyama T, Nomura M, Ogawa S, Nakanishi K. 2008. Characteristics of hydrogen bond formation between sugar and polymer in freeze-dried mixtures under different rehumidification conditions and its impact on the glass transition temperature. J Pharm Sci 97(3):1301–1312.

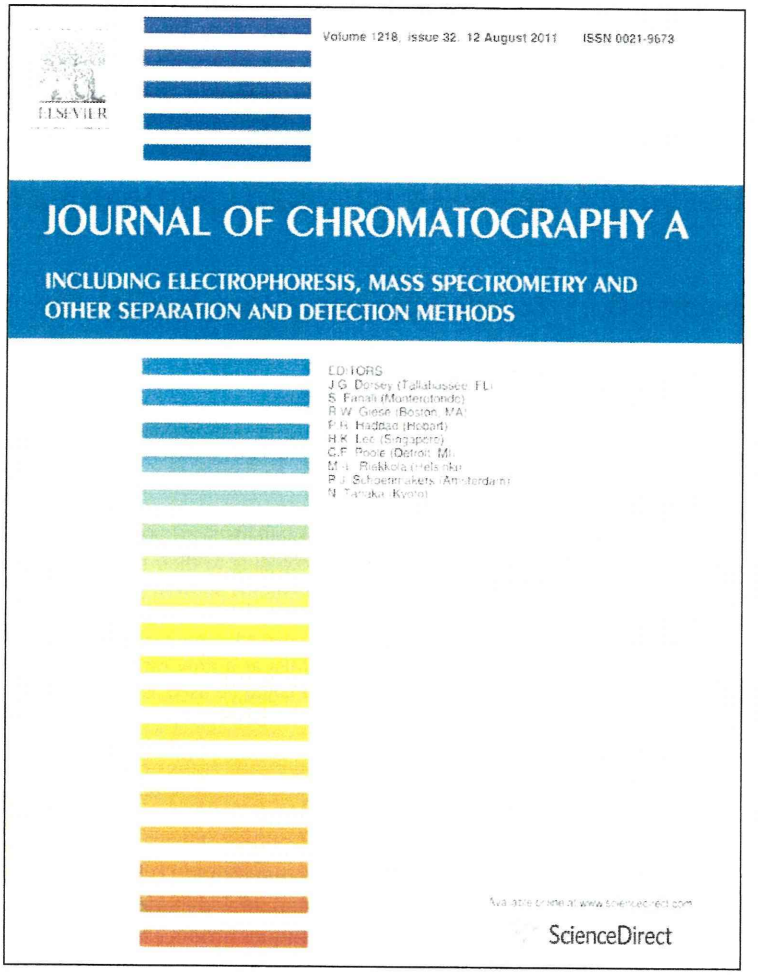

Journal of Chromatography A, 1218 (2011) 5520–5526

Contents lists available at ScienceDirect

Journal of Chromatography A

journal homepage: www.elsevier.com/locate/chroma

Size separation of colloidally dispersed nanoparticles using a monolithic capillary column

Kumiko Sakai-Kato[a,*], Shigenori Ota[b], Toyohide Takeuchi[c], Toru Kawanishi[a]

[a] Division of Drugs, National Institute of Health Sciences, 1-18-1 Kamiyoga, Setagaya-ku, Tokyo 158-8501, Japan
[b] R & D Department, GL Sciences Inc. 237-2 Sayamagahara, Iruma, Saitama 358-0032, Japan
[c] Department of Chemistry, Faculty of Engineering, Gifu University, 1-1 Yanagido, Gifu 501-1193, Japan

ARTICLE INFO

Article history:
Received 12 November 2010
Received in revised form 14 June 2011
Accepted 14 June 2011
Available online 22 June 2011

Keywords:
Nanoparticles
Monolithic column
Size exclusion chromatography

ABSTRACT

We developed a method to separate colloidally dispersed nanoparticles on monolithic capillary columns. Silica nanoparticles were eluted according to their sizes, and the plots of the logarithm of the size of nanoparticles against their elution volume showed good linearity ($r = 0.992$) over wide range of sizes. Because of the high porosity of the monolithic column (porosity; 88%), the column's length could be increased without clogging of the dispersed samples and the pressure in a long column (500 mm × 0.2 mm i.d.) was low, with a value of 5.8 MPa at a flow rate of 1 μL/min. We demonstrate that this method using monolithic capillary columns could be used as a powerful tool for size separation of nanometer-size materials, which will open a new pathway to quality control of nanomaterials in nanotechnology applications.

1. Introduction

Recent advances in nanotechnology have enabled the development of modern drug carrier systems that play an important role in the controlled delivery of pharmacological agents to their targets at a therapeutically optimal rate and dose [1]. "Soft" nanocarriers including micelles, polymers, and lipid nanoparticles have been used for drug delivery [2,3]. Carriers with greater hardness or density, including colloidally dispersed nanoparticles composed of silica, gold, or iron oxide, also have been used for drug and gene therapeutics and for diagnostic imaging [4,5]. These colloidally dispersed nanoparticles are also important in other fields: for example, gold nanoparticles have been used as imaging tools [6]; titanium dioxide particles have been used as self-cleaning, anti-bacterial agents and UV protecting agents [7,8]; and cadmium selenide has been used to create semiconductor nanocrystals (quantum dots) [9].

Exact knowledge of the size and size distribution of these nanoparticles is essential for their application in nanoparticulate drug delivery systems, because the nanoparticles' size can substantially affect their physicochemical and biopharmaceutical behavior. For example, variations in particle size can change drug release kinetics or transport phenomena across biological barriers, as well as pharmacokinetics in the human body [10–12].

Fractionation techniques offer advantages over non-fractionation techniques for particle sizing because fractionation techniques produce information about average particle size and the distribution of particle sizes for a given sample. Non-fractionation techniques, such as photon correlation spectroscopy, suffer from lower resolution than that afforded by fractionation techniques and thus are not as well suited for the analysis of samples with broad particle size distributions.

Among methods for the size analysis and characterization of macromolecules, flow-assisted techniques such as size exclusion chromatography (SEC) [13,14], hydrodynamic chromatography (HDC) [15,16], field-flow fractionation (FFF) [17–19] and capillary hydrodynamic fractionation [20] are suitable for separation of samples on the basis of differences in the physical size indexes of the analytes.

When colloids possess an electric charge in buffered aqueous solutions, electrophoretic separation methods are also among those utilized methods for particle separation and characterization. Reports have been made to employ capillary electrophoresis for analytical separations of charged particulate materials, mostly carried out by capillary zone electrophoresis [21–23].

SEC is the most commonly used fractionation method for particle sizing. Usually, SEC is performed on a column packed with polymer gel or porous silica microparticles with pore-size distributions over the range of a few to a few hundred nanometers. Polymer samples are separated with such packed SEC columns [13]. In addition, nanoparticulate drug carriers such as liposomes are often separated from small solutes by means of SEC [24].

* Corresponding author. Tel.: +81 3 3700 9662; fax: +81 3 3700 9662.
E-mail address: kumikato@nihs.go.jp (K. Sakai-Kato).

0021-9673/$ – see front matter © 2011 Elsevier B.V. All rights reserved.
doi:10.1016/j.chroma.2011.06.055

Recently, Ute et al. reported SEC of a polystyrene polymer on monolithic silica columns using tetrahydrofuran (THF) as the eluent [25]. Monolithic silica columns have received much attention as a newly introduced technology for HPLC and capillary electrochromatography [26]. These columns consist of a single piece of porous material (most often polymer- or silica-based) with a bimodal pore structure consisting of "throughpores" (pore size ~1.5–5 μm) and "mesopores in the skeleton" (~10–25 nm) [27]. Typically, monolithic columns provide higher porosity compared to conventional columns packed with spherical particles, and such higher porosity results in much lower column backpressure. Furthermore, the throughpore/skeleton size ratio of 2–4 in a monolithic column is much greater than the ratio of 0.25–0.4 typically found in a column packed with particles [28]. This increased size ratio enables the use of a long column, thus leading to high separation efficiency [29]. The sizes of the skeletons and throughpores can be independently controlled by changing the preparation conditions, including the nature of the porogen.

In this paper, we report the size separation of colloidally dispersed nanoparticles by means of a monolithic capillary column. We used monolithic columns consisting of silica derivatized with an amide group, i.e., a neutral hydrophilic bond that prohibits the adsorption of samples on the silica monolith by ion-exchange interaction and that would enable the analysis of charged soft nanocarriers such as liposomes derived from biomaterials. We analyzed the colloidal silica nanoparticles by their sizes using a monolithic capillary column. We expected that the high porosity of the monolithic columns would prevent colloidal samples from clogging the columns.

2. Materials and methods

2.1. Chemicals

Silica nanoparticles (Cataloid S) with sizes of 5, 11, 26, 45, and 78 nm were obtained from JGC Catalysts and Chemicals Ltd. (Kanagawa, Japan). Methanol (HPLC grade) and dextran standards were obtained from Sigma–Aldrich Corporation (St. Louis, MO, USA). Sodium nitrate was from Kanto Chemicals (Tokyo, Japan). Samples were dissolved or dispersed in eluent and filtered through a 0.20-μm filter (Millex-LG, Millipore Corp., Tokyo, Japan) prior to being applied to the columns. Polydiversity index (PDI) of silica nanoparticles and hydrodynamic diameters of dextran standards in eluent were measured using dynamic light scattering measurement (ZetasizerNano, Malvern, UK).

2.2. LC conditions

Sample separation was performed with a capillary LC system equipped with a capillary HPLC pump (MP711V; GL Sciences, Tokyo, Japan), a four-port internal sample injector (fixed volume: 10 nL; Valco Instrument Co. Inc., Houston, TX, USA), and a capillary ultraviolet–visible (UV–Vis) detector (MU701; GL Sciences).

Samples were analyzed on a MonoCap Amide column (500 mm × 0.2 mm; 1 μm skeleton, 2 μm throughpore, and 15 nm mesopore; GL Sciences). The permeability is represented by a K value ($K = u\varepsilon_0\eta L/\Delta P$, where u stands for the linear velocity of the eluent, ε_0 for total porosity of the column, η for solvent viscosity, L for column length, and ΔP for pressure drop [30]). Permeability was measured in 10 mM sodium phosphate buffer (pH 7.2) containing methanol (20% v/v). The total porosity of the column, ε_0 was estimated using void times of hollow capillary column and monolithic capillary column, and total volume of the column. The mobile phase consisted of a 10 mM sodium phosphate buffer (pH 7.2) containing methanol (20% v/v). The mobile phase was delivered at a rate of 0.1–1 μL/min and the column was kept at room temperature. The detector was operated at a wavelength of 210 nm. A sample volume of 10 nL was injected for each analysis. The morphology of the monolithic silica was examined by a scanning electron microscope (SEM; S-3000N, Hitachi). For the measurement of flow rate, we used a flowmeter composed of 5-μL microsyringe attached to the end of the column.

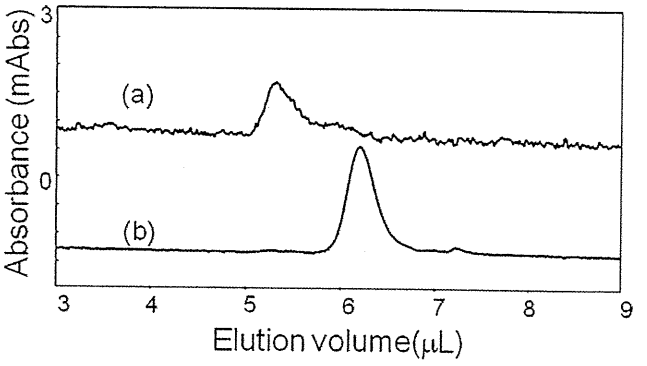

Fig. 1. Effect of eluent composition on elution profile of a sample of 26 nm silica nanoparticles. Column: Capillary EX nano Monocap Amide (250 mm × 0.2 mm i.d.); eluent: (a) water or (b) 10 mM phosphate buffer (pH 7.2); flow rate: 1 μL/min.

3. Results and discussion

Usually, SEC is performed with a column packed with polymer gel or porous silica microparticles. However, such columns could become clogged when used to separate colloidally dispersed nanoparticles with sufficient hardness or high density, such as inorganic nanoparticles. Therefore, in this study monolithic capillary columns with high porosity were used for the analysis of colloidally dispersed nanoparticles.

3.1. Detection

In this study, we used different sizes of silica nanoparticles. The detection method used was based on turbidimetric detection, in which colloidal species are observed with a UV–Vis detector [31,32]. Although silica nanoparticles do not contain any chromophores, it is expected that a portion of incident UV light is scattered by the silica nanoparticles, thereby reducing the intensity of light reaching the photomultiplier. This reduction in light intensity provides an apparent absorption value. In this experiment, we used different concentrations of silica nanoparticles depending on their sizes, because the larger the silica colloid, the larger the pseudo-UV absorbance observed. To achieve an optimal signal-to-noise ratio, the detector wavelength was set to 210 nm for the experiments described here.

3.2. Optimization of eluent

It is important that the silica nanoparticles maintain a consistent size during analysis; therefore, an eluent should be chosen that does not cause gelation, aggregation, or dissolution of the particles. As shown by the unstable baseline and small sample peak in Fig. 1(a), water was not appropriate as an eluent compared with phosphate buffer (Fig. 1(b)). It is considered that the silica nanoparticles probably are not stable and coagulated in plain water, and silica nanoparticles are prone to clogging injectors or columns which lead to small peak area in plain water [33]. For these reasons we used phosphate buffer as the eluent in our studies.

We also examined the effect of the eluent pH on the peak area and plate number of silica nanoparticles. We used 10 mM phos-

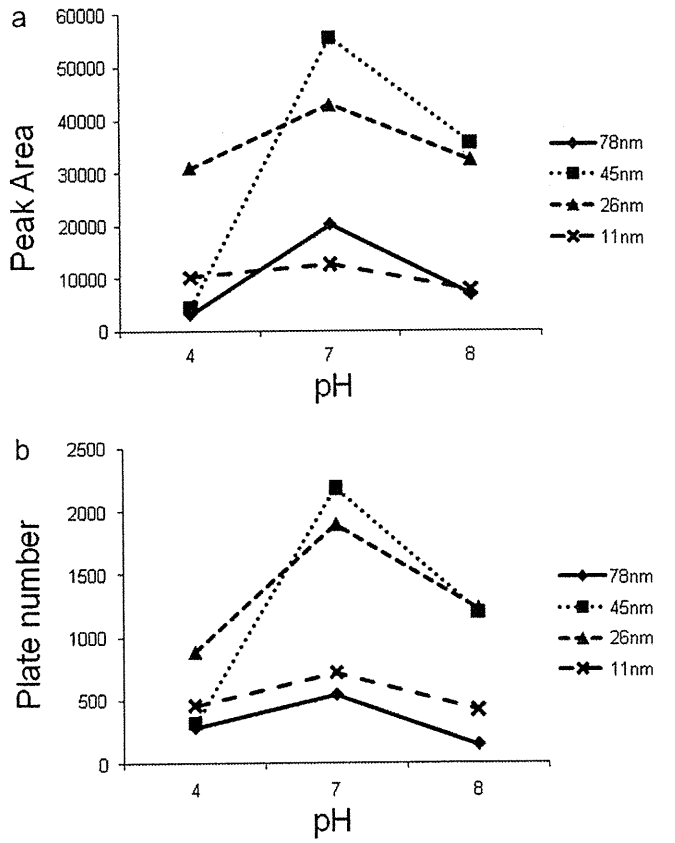

Fig. 2. Effect of eluent pH on (a) peak area and (b) plate number of various sizes of silica nanoparticles. Eluent: 10 mM phosphate buffer (pH 4, 7.2, or 8); sample: 0.3% (w/v) 78 nm, 0.5% (w/v) 45 nm, 1% (w/v) 26 nm, and 1% (w/v) 11 nm silica nanoparticles. Each sample containing one size of particles. Other conditions are the same as those described in Fig. 1.

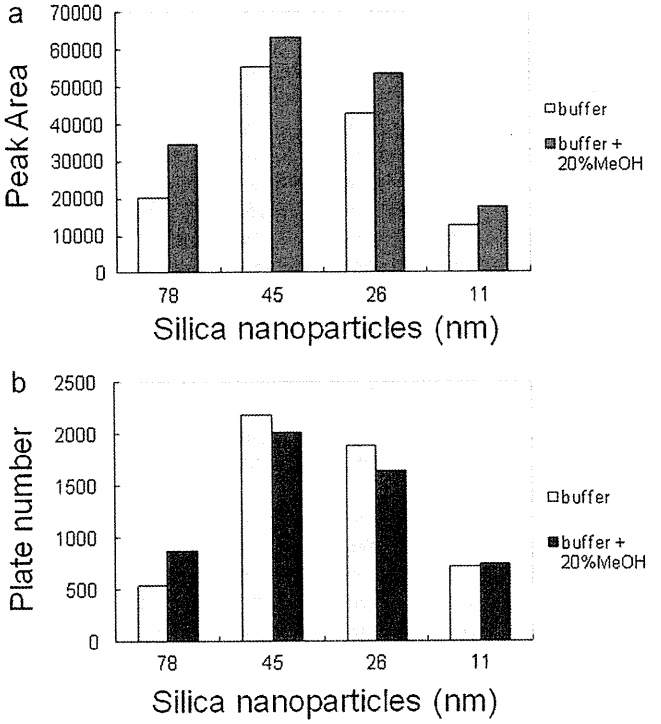

Fig. 3. Effect of methanol ratio in the eluent on (a) peak area and (b) plate number of various sizes of silica nanoparticles. Eluent: 10 mM phosphate buffer (pH 7.2) or 10 mM phosphate buffer (pH 7.2) containing 20% methanol. The other chromatographic conditions were the same as in Fig. 2.

phate buffer at pH 4, 7.2, and 8. As shown in Fig. 2, both the peak area and the plate number were the largest at pH 7.2 for all sizes of silica nanoparticles. It is probable that coagulation of silica nanoparticles takes place at lower pH, due to a decrease in electrostatic repulsion, and silica nanoparticles are prone to clogging injectors or columns which lead to small peak area in plain water. Considering the above results and the stability of the separation column, we used phosphate buffer at pH 7.2 in our studies.

Examining the effect of phosphate buffer concentration on sample peak size, we found that the sample peak area was larger in 10 mM phosphate buffer than it was in 50 mM phosphate buffer. This difference was most pronounced for the sample of 78-nm silica nanoparticles (data not shown). The decrease in peak area with increasing buffer concentration was probably caused by nanoparticle coagulation that would have been induced by high concentrations of sodium cations in the buffer [34]. Therefore, we used 10 mM phosphate buffer (pH 7.2) in our experiments.

Finally, we examined the effect of organic solvent on sample peak area. Because slightly larger peak areas were observed with methanol than with acetonitrile, we selected methanol as an organic solvent (data not shown). This preference for methanol may be ascribed to a different hydrogen bonding force between silica nanoparticles and methanol or acetonitrile. By adding methanol at 20% (v/v) to the eluent, peak areas of all sample peaks were increased; however, the plate number did not increase for all sizes of nanoparticles (Fig. 3). Further increases in the organic solvent ratio up to 90% (v/v) largely decreased the peak area. This observed decrease in peak area with increasing organic solvent ratio probably occurred because the presence of the solvent decreased the electric double layer around the nanoparticles, which would have resulted in the reduction of repulsion between each nanoparticle and thus increased particle aggregation. Therefore, 20% methanol was added to the phosphate buffer in our experiments. When 10 mM phosphate buffer (pH 7.2) containing 20% methanol was used as the eluent, the pressure in a long column (500 mm × 0.2 mm i.d.) was low, with a value of 5.8 MPa at a flow rate of 1 μL/min. Under this condition, the permeability K was 6.7×10^{-14} m^2 and the total porosity of the column was 88%.

3.3. *Effect of column length and flow rate on silica nanoparticle separation*

The use of longer monolithic columns would be one possible way to better separate mix samples. Fig. 4(a) shows the effect of column length on column efficiency for silica nanoparticles with different sizes. We used 150, 250, and 500 mm columns; these are all that are commercially available. The column efficiency slightly increased with column length for all silicate nanoparticles using the same eluent and flow rate (1 μL/min). This result is probably explained by the external-band broadening contributions [35]. The contribution of external-band broadening contributions to total system efficiency was larger as the column length decreased and the ratio of extra-column variance to total system variance were 37, 54, 78%, when nanoparticles of size of 78 nm were analyzed onto 500, 250, and 150 mm columns, respectively. The extra-column variance was calculated by measuring the half bandwidth of nanoparticle peak analyzed without column. Although using a longer column takes a longer time to elute solutes, it has an advantage for better separation of a mixture sample, In fact, as shown in Fig. 4(b), the separation of silica nanoparticles mixture was gradually improved by using longer column length, although the elution time is getting longer.

Further, we examined the effect of flow rate on column efficiency to improve the separation of the silica nanoparticle mixture. We confirmed the accuracy and precision of flow rate with various

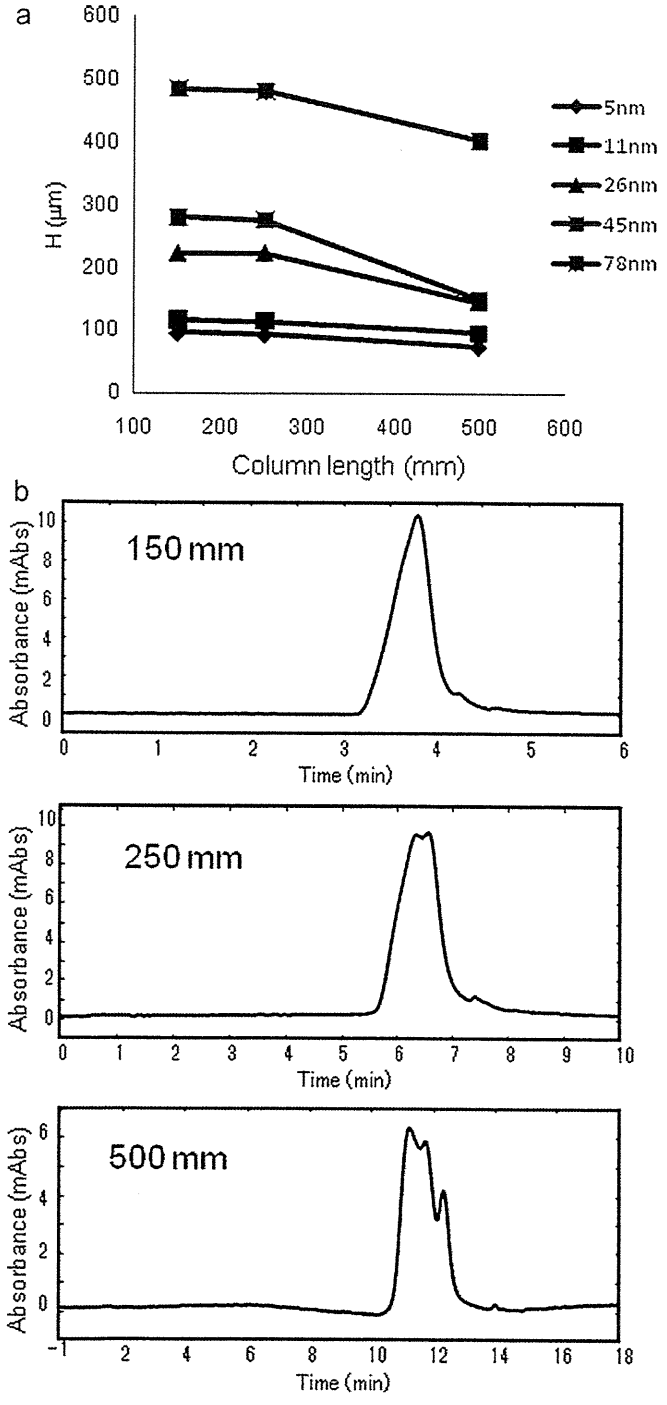

Fig. 4. Effect of column length on (a) plate number and (b) silica nanoparticle separation. Column: Capillary EX nano Monocap Amide (150, 250, and 500 mm × 0.2 mm i.d.); eluent: 10 mM phosphate buffer (pH 7.2) containing 20% methanol; sample: (a) 0.3% (w/v) 78 nm, 0.5% (w/v) 45 nm, 1% (w/v) 26 nm, 1% (w/v) 11 nm, 2% (w/v) 5 nm silica nanoparticles, (b) mixture of 1% (w/v) 78 nm, 2.8% (w/v) 26 nm, 10% (w/v) 5 nm. Flow rate: 1 μL/min.

flow rate settings using a flow meter at the outlet of the column, and proved the accuracy and precision of flow rate including low flow rate we used in our report (Table 1). We also confirmed that the silica nanoparticles have a narrow distribution suitable for assessment of column efficiency. We measured the polydiversity index (PDI) of each silica nanoparticle by dynamic light scattering. The PDI value is an estimate of the distribution width and for a narrow distribution, a PDI of around 0.1 or lower is expected. The PDI values were 0.018 (78 nm silica), 0.022 (45 nm), 0.053 (26 nm),

Table 1
Accuracy and precision of flow rate.

	Flow (μL/min)					
	3	2	1	0.5	0.2	0.1
Mean	2.972	1.991	0.999	0.497	0.200	0.0996
SD	0.0157	0.0083	0.0037	0.0023	0.0004	0.0003
Precision (%)	0.53	0.42	0.37	0.47	0.18	0.28
Accuracy (%)	99.08	99.56	99.93	99.30	99.81	99.59

Flow rate was measured using a flow meter according to the manufacturer's protocol. Column: Capillary EX nano Monocap Amide (500 mm × 0.2 mm i.d.); eluent: 10 mM phosphate buffer (pH 7.2) containing 20% methanol.

0.085 (11 nm), 0.169 (5 nm). Although, PDI value of 5-nm silica nanoparticle was a little larger than 0.1, the distribution of other nanoparticles was narrow according to PDI values.

In SEC, for discussion of the effect of flow rate on plate height (H), Giddings' coupling theory can be simply represented by [36]

$$H = \frac{1}{(1/A)+(1/Eu)} + \frac{B}{u} + Cu. \quad (1)$$

In this equation, u is the eluent linear velocity, and A, B, C, and E are coefficients that contribute to band broadening and thus to H. The contribution of each of the terms in Eq. (1) to H are functions of (1) the coupling effect of eddy diffusion, A term (a simple flow-splitting phenomenon that is not expected to vary with linear velocity) and lateral diffusion, E term (extraparticle mass transfer in case of packed column), (2) longitudinal diffusion, B term, and (3) mass transfer, C term (solute diffuse in and out the pores and stationary-phase mass transfer effect involving basic sorption–desorption process). The curves of H *versus* u are shown in Fig. 5(a) and part of this graph was enlarged in Fig. 5(b). For sodium nitrate, the plate height is mainly determined by longitudinal molecular diffusion, which is a result of the relatively high values of B term (proportional to molecular diffusion coefficient). This causes H to increase drastically with low-velocity regions as shown in Fig. 5(b). On the other hand, the longitudinal effect (2) is generally insignificant for macromolecules, band broadening is controlled by mass transfer terms (3) or by coupling effects of eddy diffusion and lateral diffusion (1). For the mass transfer processes (C term), the magnitude of the C term is dependent on the rate of diffusion of solute in and out of the pore structure. Therefore, larger, slower-diffusing molecules increase the value of the C term more than do smaller, faster-diffusing molecules [37]. In fact, as shown in Fig. 5(a), the H *versus* u curves of silica nanoparticles were almost linear ($r = 0.993$–0.998) over the whole range we examined, which is different from sodium nitrate, as reported using porous silica particle columns [38]. Furthermore, the slopes of linear curves increased with an increase in the particle sizes. These results indicate that C term is a dominant plate-height term for silica nanoparticles analysis on a monolithic column.

From Fig. 5, we expected that a decrease in u should decrease H and thus increase peak resolution. In the present study, the peak resolution improved with decreasing flow rate when a mixture of different sizes of silica nanoparticles (78, 26, and 5 nm) were analyzed on a 500 mm × 0.2 mm i.d. capillary monolithic column (Fig. 6). As shown in Fig. 6, an increase in peak resolution was observed with a decrease in flow rate. The shift of peaks by the decrease in flow rate was presumably caused by an increase in permeation for nanoparticles into porous structure of silica monolith. At a flow rate of 0.1 μL/min, some aggregates were detected that were not observed at faster flow rates. A similar increase in resolution also has been reported for a mixture of proteins separated at various flow rates on a silicagel-packed column [39].

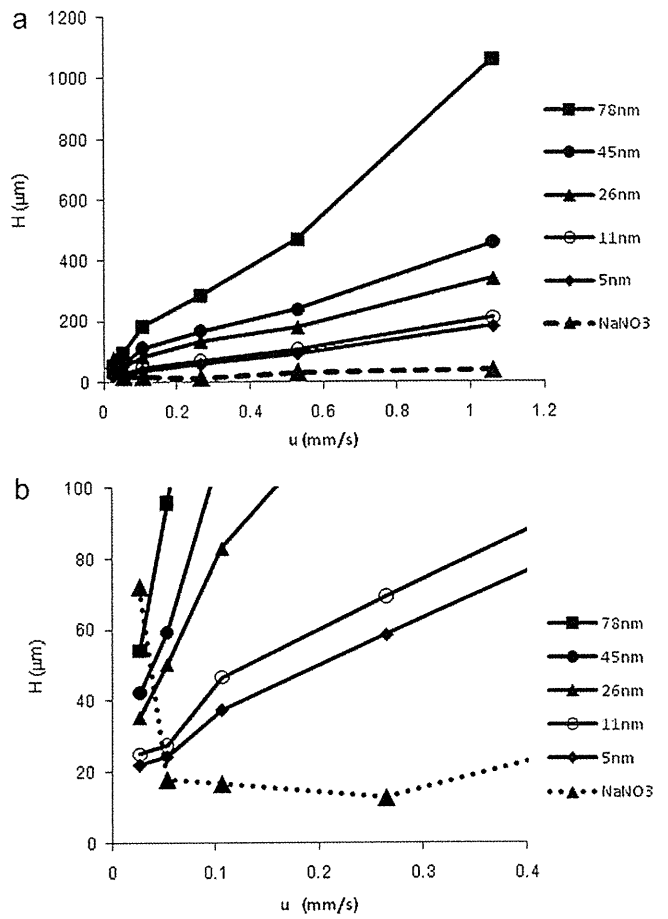

Fig. 5. (a) Plots of plate height (H) values against linear velocity of eluent (u) and (b) its low velocity region. Column: Capillary EX nano Monocap Amide (500 mm × 0.2 mm i.d.); eluent: 10 mM phosphate buffer (pH 7.2) containing 20% methanol; sample: 0.3% (w/v) 78 nm, 0.5% (w/v) 45 nm, 1% (w/v) 26 nm, 1% (w/v) 11 nm, 2% (w/v) 5 nm silica nanoparticles, and 10 μg/mL sodium nitrate.

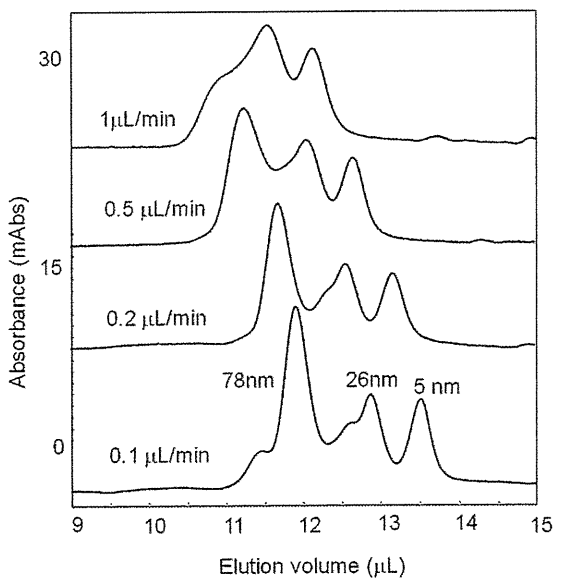

Fig. 6. Effect of flow rate on peak resolution of silica nanoparticles. Column: Capillary EX nano Monocap Amide (500 mm × 0.2 mm i.d.); eluent: 10 mM phosphate buffer (pH 7.2) containing 20% methanol; sample: mixture of 1% (w/v) 78 nm, 2.8% (w/v) 26 nm, and 10% (w/v) 5 nm silica nanoparticles; flow rate: 1, 0.5, 0.2, or 0.1 μL/min. The other conditions were the same as described in Fig. 1.

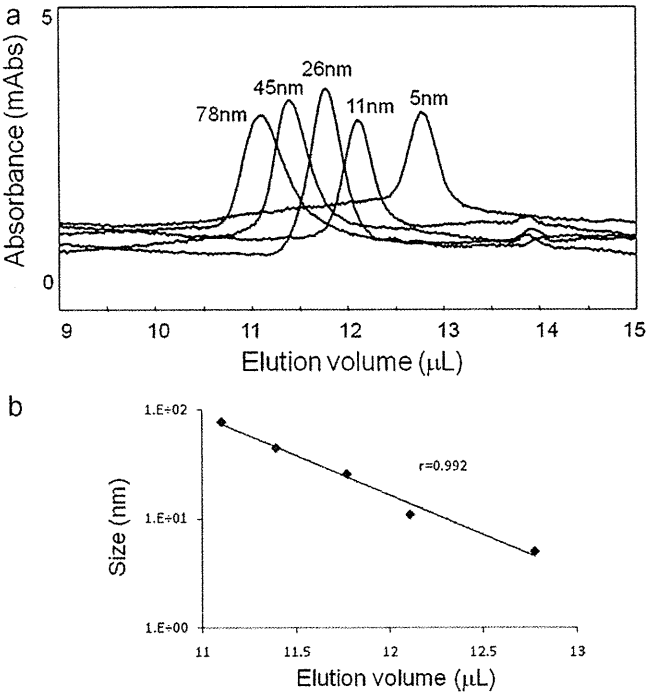

Fig. 7. (a) Particle size distribution overlay plot for five sizes of silica nanoparticles and (b) plot of the logarithm of the mass of 1 mol particles as a function of elution volume for each size of silica nanoparticles. Column: Capillary EX nano Monocap Amide (500 mm × 0.2 mm i.d.); flow rate: 0.5 μL/min; samples: solutions of 0.3% (w/v) 78 nm, 0.5% (w/v) 45 nm, 1% (w/v) 26 nm, 2% (w/v) 11 nm, and 1.5% (w/v) 5 nm silica nanoparticles. The other conditions were the same as described in Fig. 4.

3.4. Calibration curve

Fig. 7(a) shows an overlay of the particle size distribution obtained for five different samples. The nanoparticles were eluted in order of decreasing size. The logarithm of size of nanoparticles was plotted against its elution volume (Fig. 7(b)).

The plot was almost linear (r = 0.992) over a wide range of sizes including a very large size region beyond the size of mesopores (15 nm). Because SEM micrographs show the presence of very rough surfaces of the monolithic silica support in micron and submicron ranges (Fig. 8), our result indicates that not only mesopores but also these rough structures contribute to the size separation of silica nanoparticles.

We further explored the separation mechanism by drawing the molecular weight *versus* elution volume plot using dextran standards because silica nanoparticles with low molecular weight cannot be obtained. As shown in Fig. 9, the plot was linear at the high molecular weight region. Because the average hydrodynamic size of the largest dextran standard is 48 nm, this result indicates that the wide pore size distribution of the monolithic structure contributes to the selective permeation for a wide range of dextran standards and that size separation is possible beyond the range provided by the mesopores. Fig. 9 also shows that the plot curves at the low molecular weight region of below about 1000, which indicates that the permeation limit of this column exists as SEC mode.

Others also have reported that the separation of polystyrene standards according to molecular weight apparently occurred not only in the mesopores of a silica monolith (internal pore zone) but also at the outside (external pore zone) [25,40]. Ute et al. reported that when polystyrene standards were separated on a monolithic capillary column, the resulting calibration curve was linear over a wide range of masses as shown here [25]. We also examined the repeatability of the elution times using 26 and 76 nm silica nanoparticles, and relative standard deviations of the elution

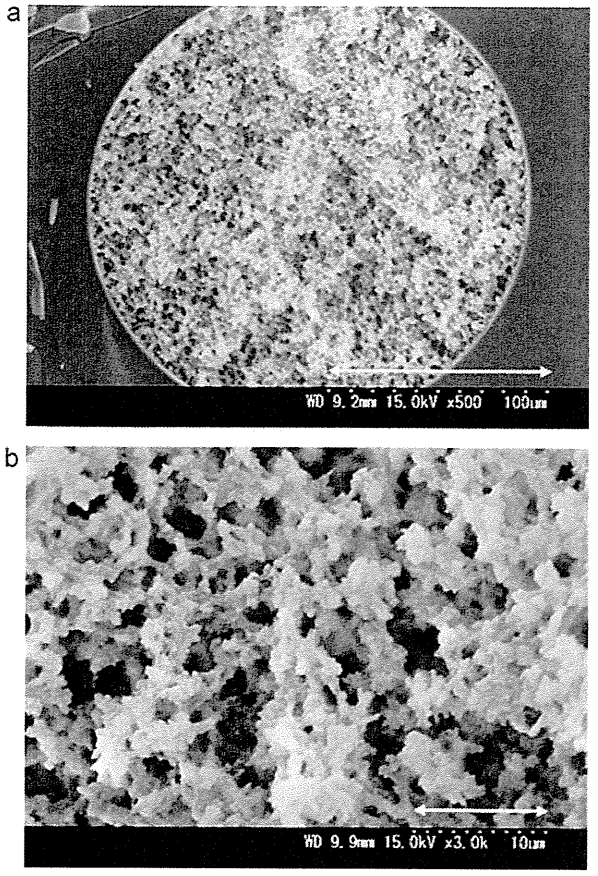

Fig. 8. Scanning electron micrographs of monolithic silica capillary columns. Scale bars corresponding to 100 μm for (a) and 10 μm for (b).

times were 0.24 and 0.15% ($n = 3$), respectively. The good linearity and repeatability of elution observed in our study indicates that this monolithic column can be used with minimal unfavorable adsorption of the solute on the column skeleton and can be used for knowledge of size and size distribution of nanoparticle samples using the calibration curve. This minimal adsorption is ascribed to alteration of the silica surface by organic functional groups. By modifying the size of mesopores or throughpores in monolithic columns, it would be possible to further clarify the separation mechanism and design columns to resolve nanoparticles with wide size ranges. Also, quantitative evaluation of particle size distribution using chromatograms remains to be solved.

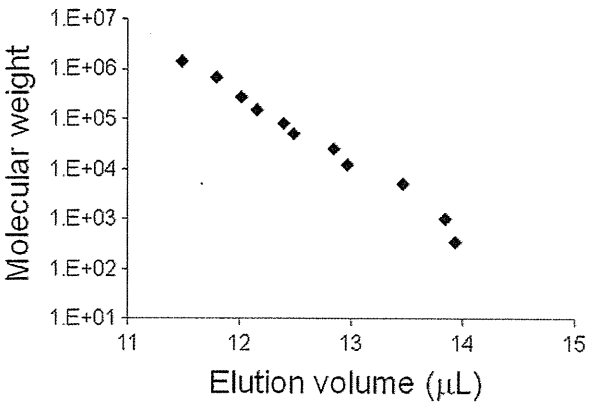

Fig. 9. Selective permeation of dextran standards. Column: Capillary EX nano Monocap Amide (500 mm × 0.2 mm i.d.); eluent: 10 mM phosphate buffer (pH 7.2) containing 20% methanol; flow rate: 1 μL/min.; sample: dextran standard; detection: UV190 nm.

4. Conclusions

In this study, we used a monolithic capillary column to develop a novel technique for the highly resolved separation of colloidally dispersed nanoparticles by their sizes. Because the column had a low backpressure, an increase in resolution could easily be achieved by elongating the column length. By optimizing the flow rate in the column, we resolved nanoparticles with only slight differences in size. The molecular weight *versus* elution volume plot curves at the low molecular weight region of below about 1000, which indicates that the permeation limit of this column exists as SEC mode. In future studies, the effect of these monolithic column structures (the sizes of mesopores and throughpores) on nanoparticle separation should be further explored to clarify the details of separation mechanism. This separation method represents a powerful means of size distribution for quality control of manufactured nanotechnology medicinal products, and this method can also be used to detect these products' impurities, including their aggregates. Therefore, this method could be used to analyze other industry-important dispersed nanomaterials, including carbon nanotubes or fullerenes.

Acknowledgements

The authors are grateful for financial support from the Research on Publicly Essential Drugs and Medical Devices Project (The Japan Health Sciences Foundation), a Health Labor Sciences Research Grant from the Ministry of Health, Labor and Welfare (MHLW), and KAKENHI (21790046) from the Ministry of Education, Culture, Sports, Science, and Technology (MEXT), Japan. The authors thank Eisai Co., Ltd. for fruitful discussion.

References

[1] M. Ferrari, Nat. Rev. Cancer 5 (2005) 161.
[2] R. Duncan, Nat. Rev. Cancer 6 (2006) 687.
[3] V.P. Torchilin, Nat. Rev. Drug Discov. 4 (2005) 145.
[4] C. Barbé, J. Bartlett, L. Kong, K. Finnie, H.Q. Lin, M. Larkin, S. Calleja, A. Bush, G. Calleja, Adv. Mater. 16 (2004) 1959.
[5] I.I. Slowing, B.G. Trewyn, S. Giri, V.S.-Y. Lin, Adv. Funct. Mater. 17 (2007) 1225.
[6] Z.Y. Zhong, K.B. Male, J.H.T. Luong, Anal. Lett. 36 (2003) 3097.
[7] K. Han, M. Yu, J. Appl. Polym. Sci. 100 (2006) 1588.
[8] R. Dastjerdi, M. Montazer, Colloids Surf. B: Biointerfaces 79 (2010) 5.
[9] C.B. Murray, D.J. Norris, M.G. Bawendi, J. Am. Chem. Soc. 115 (2002) 625.
[10] J.F. Hillyer, R.M. Albrecht, J. Pharm. Sci. 90 (2001) 1927.
[11] A. Lamprecht, Y. Bouligand, J.P. Benoit, J. Control. Release 84 (2002) 59.
[12] J. Rejman, V. Oberle, I.S. Zuhorn, D. Hoekstra, Biochem. J. 377 (2004) 159.
[13] J.J. Kirkland, J. Chromatogr. 125 (1976) 231.
[14] S.S. Huang, C.-S. Wu (Eds.), Handbook of Size Exclusion Chromatography and Related Techniques, Marcel Dekker, New York, 2004, p. 677.
[15] H. Small, J. Colloid Interface Sci. 48 (1974) 147.
[16] A. Williams, E. Varela, E. Meehan, K. Tribe, Int. J. Pharm. 242 (2002) 295.
[17] J.C. Giddings, Science 260 (1993) 1456.
[18] J.C. Giddings, Anal. Chem. 67 (1995) 592A.
[19] M.H. Moon, I. Park, Y. Kim, J. Chromatogr. A 813 (1998) 91.
[20] C.A. Silebi, J.G. Dosramos, J. Colloid. Interface Sci. 130 (1989) 14.
[21] B.B. VanOrman, G.L. McIntire, J. Microcolumn Sep. 1 (1989) 289.
[22] H. Ahmadzadeh, R. Dua, A.D. Presley, E.A. Arriaga, J. Chromatogr. A 1064 (2005) 107.
[23] Y.H. Rezenom, A.D. Wellman, L. Tilstra, C.D. Medley, S.D. Gilman, Analyst 132 (2007) 1215.
[24] C. Grabielle-Madelmont, S. Lesieur, M. Ollivon, J. Biochem. Biophys. Methods 56 (2003) 189.
[25] K. Ute, S. Yoshida, T. Kitayama, T. bamba, K. Harada, E. Fukusaki, A. Kobayashi, N. Ishizuka, H. Minakuchi, K. Nakanishi, Polym. J. 38 (2006) 1194.
[26] H. Minakuchi, K. Nakanishi, N. Soga, N. Ishizuka, N. Tanaka, Anal. Chem. 68 (1996) 3498.
[27] N. Tanaka, H. Kobayashi, K. Nakanishi, H. Minakuchi, N. Ishizuka, Anal. Chem. 73 (2001) 420A.
[28] K.K. Unger, Porous Silica; Journal of Chromatography Library, vol. 16, Elsevier, Amsterdam, 1979.

[29] K. Miyamoto, T. Hara, H. Kobayashi, H. Morisaka, D. Tokuda, K. Horie, K. Koduki, S. Makino, O. Núñez, C. Yang, T. Kawabe, T. Ikegami, H. Takubo, Y. Ishi hama, N. Tanaka, Anal. Chem. 80 (2008) 8741.
[30] G. Guiochon, J. Chromatogr. A 1168 (2007) 101.
[31] A. Zattoni, E.L. Piccolomini, G. Torsi, P. Reschiglian, Anal. Chem. 75 (2003) 6469.
[32] Z. Aspanut, T. Yamada, L.W. Lim, T. Takeuchi, Anal. Bioanal. Chem. 391 (2008) 353.
[33] T. Takeuchi, Siswoyo, Z. Aspanut, L.W. Lim, Anal. Sci. 25 (2009) 301.
[34] J. Depasse, A. Watillon, J. Colloid Interface Sci. 33 (1970) 430.
[35] F. Gritti, C.A. Sanchez, T. Farkas, G. Guichon, J. Chromatogr. A 1217 (2010) 3000.
[36] J.C. Giddings, Dynamics of Chromatography: Principles and Theory, Marcel Dekker, New York, 1965, p. 62.
[37] A. Striegel, W.W. Yau, J.J. Kirkland, D.D. Bly, Modern Size-Exclusion Liquid Chromatography: Practice of Gel Permeation and Gel Filtration Chromatography, John Wiley and Sons, Inc., New Jersey, 2009, p. 55.
[38] G. Stegeman, J.C. Kraak, H. Poppe, J. Chromatogr. 550 (1991) 721.
[39] H. Engelhardt, U.M. Schon, Chromatographia 22 (1986) 388.
[40] M. Al-Bokari, D. Cherrak, G. Guiochon, J. Chromatogr. A 975 (2002) 275.

International Journal of Pharmaceutics 407 (2011) 111–118

Contents lists available at ScienceDirect

International Journal of Pharmaceutics

journal homepage: www.elsevier.com/locate/ijpharm

Differences in crystallization rate of nitrendipine enantiomers in amorphous solid dispersions with HPMC and HPMCP

Tamaki Miyazaki[a,*], Yukio Aso[a], Sumie Yoshioka[b], Toru Kawanishi[a]

[a] Division of Drugs, National Institute of Health Sciences, 1-18-1 Kamiyoga, Setagaya-ku, Tokyo 158-8501, Japan
[b] School of Pharmacy, University of Connecticut, Storrs, CT, United States

ARTICLE INFO

Article history:
Received 21 October 2010
Received in revised form
21 December 2010
Accepted 19 January 2011
Available online 26 January 2011

Keywords:
Nitrendipine
Enantiomer
Chiral polymer
Solid dispersions
Crystallization

ABSTRACT

To clarify the contribution of drug–polymer interaction to the physical stability of amorphous solid dispersions, we studied the crystallization rates of nitrendipine (NTR) enantiomers with identical physicochemical properties in the presence of hydroxypropylmethylcellulose (HPMC), hydroxypropylmethylcellulose phthalate (HPMCP) and polyvinylpyrrolidone (PVP). The overall crystallization rate at 60 °C and the nucleation rate at 50–70 °C of (+)-NTR were lower than those of (−)-NTR in the presence of 10–20% HPMC or HPMCP. In contrast, similar crystallization profiles were observed for the NTR enantiomers in solid dispersions containing PVP. The similar glass transition temperatures for solid dispersions of (−)-NTR and (+)-NTR suggested that the molecular mobility of the amorphous matrix did not differ between the enantiomers. These results indicate that the interaction between the NTR enantiomers and HPMC or HPMCP is stereoselective, and that differences in the stereoselective interaction create differences in physical stability between (−)-NTR and (+)-NTR at 50–70 °C. However, no difference in physical stability between the enantiomers was obvious at 40 °C. Loss of the difference in physical stability between the NTR enantiomers suggests that the stereoselective interaction between NTR and the polymers may not contribute significantly to the physical stabilization of amorphous NTR at 40 °C.

1. Introduction

Nifedipine analogues are used for treatment of cardiovascular disorders. Most of them are poorly water soluble and their bioavailability is low when administered orally in crystal form. To improve the bioavailability by increasing the dissolution rate and solubility, amorphous solid dispersions of nifedipine analogues have been studied over the past few decades (Suzuki and Sunada, 1998; Chutimaworapan et al., 2000; Vippagunta et al., 2002; Hirasawa et al., 2003a,b, 2004; Tanno et al., 2004; Karavas et al., 2005, 2006; Wang et al., 2005, 2007; Kim et al., 2006; Konno and Taylor, 2006; Huang et al., 2008; Marsac et al., 2008; Rumondor et al., 2009a,b). Drugs in an amorphous state are more easily dissolved in water than their crystalline counterparts. However, recrystallization to a thermodynamically stable form during long-term storage is a matter of concern. The physical stability of amorphous solid dispersions (crystallization tendency) has been reported to correlate with several factors, such as molecular mobility (Aso et al., 2004; Miyazaki et al., 2007), drug–excipient interactions and miscibility (Matsumoto and Zografi, 1999; Marsac et al., 2006, 2009; Miyazaki et al., 2004, 2006, 2007; Konno and Taylor, 2006; Haddadin et al., 2009; Tao et al., 2009; Telang et al., 2009). The crystallization rate of amorphous nitrendipine (NTR) increases with a decrease in the glass transition temperature (T_g) associated with water sorption, indicating that molecular mobility, in terms of T_g, is correlated with physical stability. However, amorphous nilvadipine is more stable than nifedipine, even though the two had similar T_g values, indicating that the difference in physical stability between nilvadipine and nifedipine might be attributable to differences in chemical structure (Miyazaki et al., 2007). Hydrogen bond interaction between felodipine and hydroxypropylmethylcellulose (HPMC) or hydroxypropylmethylcellulose acetate succinate is considered to decrease the nucleation rate of felodipine, since no significant change in molecular mobility, reflected in T_g value, has been observed (Konno and Taylor, 2006). Also, drug–excipient miscibility is reportedly related to the physical stability of nifedipines. Drug crystallization has been observed to occur earlier in solid dispersions showing phase separation due to low miscibility of the drug with the excipient polymers (Rumondor et al., 2009a,b; Marsac et al., 2010). In order to develop stable amorphous solid dispersions, it is important to clarify the relative significance of these factors for the physical stability of amorphous solid dispersions. Therefore, designing a model system that is as simple as possible is the key to evaluation of each individual factor.

NTR has an asymmetric carbon (Fig. 1), and is available as a mixture of both enantiomers. These enantiomers can be resolved by chiral chromatography. Since both enantiomers have identical physical and chemical properties, including molecular mass, T_g,

* Corresponding author. Tel.: +81 3 3700 1141; fax: +81 3 3707 6950.
E-mail address: miyazaki@nihs.go.jp (T. Miyazaki).

0378-5173/$ – see front matter © 2011 Elsevier B.V. All rights reserved.
doi:10.1016/j.ijpharm.2011.01.035

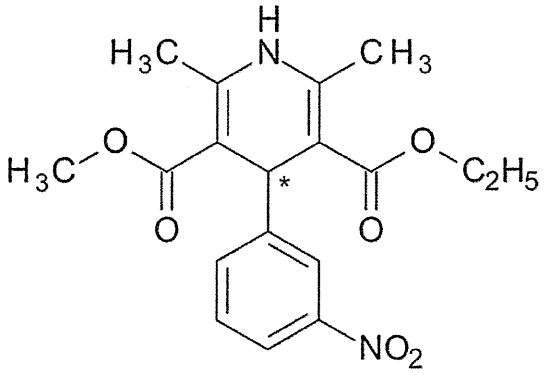

Fig. 1. Chemical structure of NTR. The asterisk represents asymmetric carbon.

melting point and density, the effects of molecular mobility and chemical structure on their physical stability are expected to be the same. Therefore, solid dispersions of NTR enantiomers may provide a useful model system for studies of drug–polymer stereoselective interaction. In the present study, HPMC and hydroxypropylmethylcellulose phthalate (HPMCP) were used as chiral polymers, and polyvinylpyrrolidone (PVP), an achiral polymer, was selected as a control to investigate the effect of drug–polymer interaction on the physical stability of amorphous NTR enantiomers. The overall crystallization rates were determined from the time-profiles of amorphous drug remaining, as measured by differential scanning calorimetry (DSC). Furthermore, the nucleation and the crystal growth rates of each NTR enantiomer in the solid dispersions containing HPMC, HPMCP or PVP were determined by polarized light microscopy. Measurements of T_g and Fourier-transform infrared spectra (FT-IR) were carried out for evaluation of molecular mobility and drug–polymer interactions, respectively.

2. Materials and methods

2.1. Materials

PVP (PVP10) and HPMC (USP grade) were purchased from Sigma–Aldrich, Inc. HPMCP (HP-55) was kindly obtained from Shin-Etsu Chemical Co., Ltd.

NTR (Wako Pure Chemical Industries Ltd.) was resolved on a CHIRALCEL OJ-H column (Daicel Chemical Industries, Ltd., 10 mm × 250 mm) into two fractions of each enantiomer with a mobile phase of n-hexane/ethanol (100/15, flow rate: 4 ml/min). A 500 μl of 1% NTR solution in n-hexane/ethanol (1/1) was injected, and ultraviolet spectrophotometric detection was carried out at 254 nm. The circular dichroism spectrum of the first fraction exhibited a negative peak at around 360 nm, and the second one exhibited a positive peak. Therefore, the first and second fractions of NTR were designated (−)-NTR and (+)-NTR, respectively. The optical purity of each enantiomer was determined to be more than 99.96%, and the amount of photo degradation product of NTR was determined to be less than 0.03% by liquid chromatography, on a CHIRALCEL OJ-H column (Daicel Chemical Industries, Ltd.,

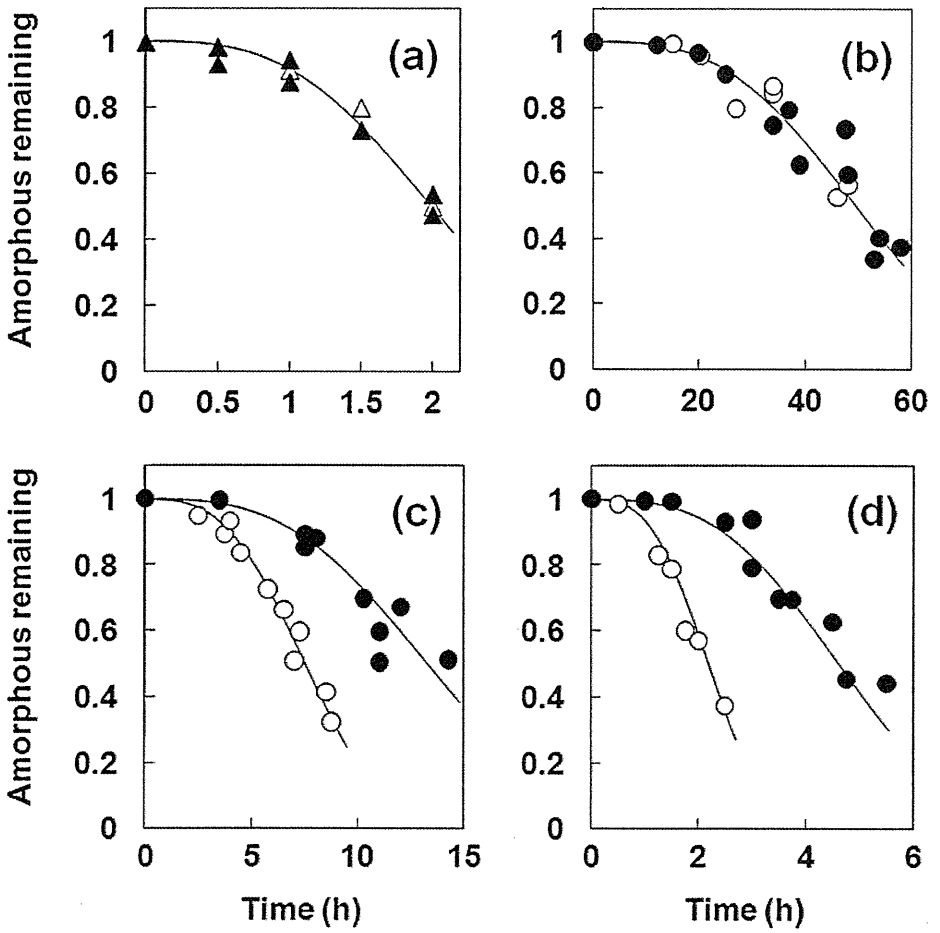

Fig. 2. Crystallization profiles of each NTR enantiomer alone ((a): △, ▲) and the enantiomers in solid dispersions (○, ●) with (b) 10% PVP, (c) 10% HPMC and (d) 10% HPMCP at 60 °C. Open symbols represent (−)-NTR and solid symbols represent (+)-NTR. The lines in the figures represent the best fit of the Avrami equation.

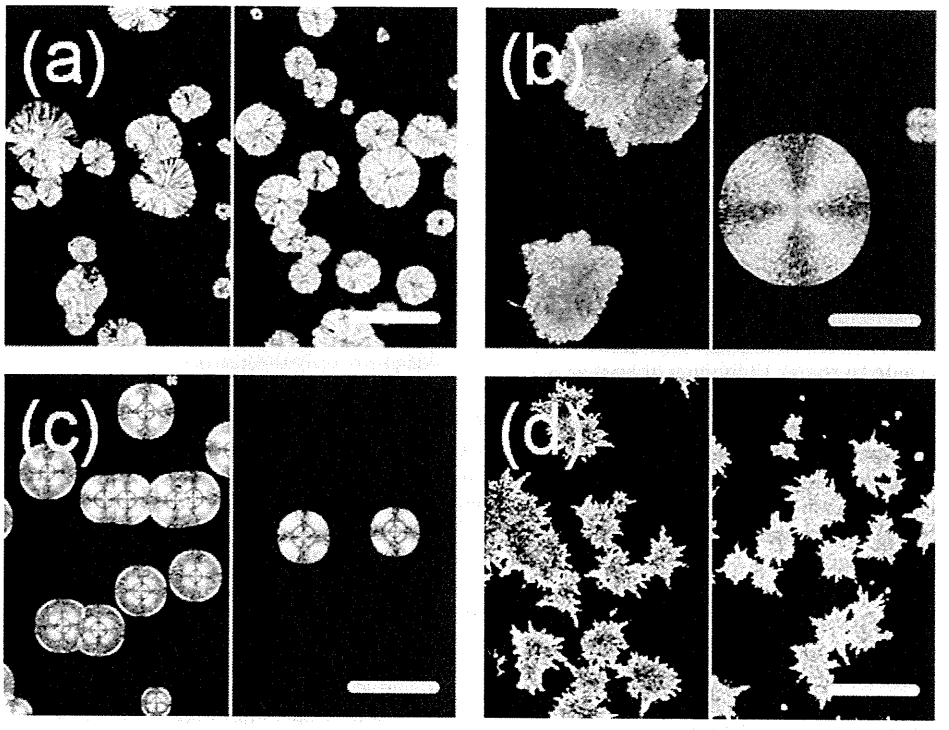

Fig. 3. Typical crystal shape observed for the amorphous NTR enantiomers and their solid dispersions: (a) without polymer, (b) 10% HPMC, (c) 10% HPMCP and (d) 10% PVP. The left side of each micrograph was taken from the (−)-NTR samples, and the right side from the (+)-NTR samples. The bars in the micrographs correspond to 100 μm.

4.6 mm × 250 mm) with a mobile phase of n-hexane/ethanol = 10/1 (1 ml/min). Since NTR is a photo sensitive compound, NTR samples were handled under dim light (<120 lx).

2.2. Determination of the overall crystallization rate of amorphous NTR enantiomers

Amorphous solid dispersions of the NTR enantiomers were prepared by melt-quenching drug–polymer mixtures. One NTR enantiomer and a polymer were initially dissolved in a solvent that was suitable for both components. Ethanol/acetone (1:1) was used for the NTR–HPMC and NTR–HPMCP combinations, and ethanol was used for the NTR–PVP combination. Next, the solvent was rotary-evaporated to obtain a homogeneous drug–polymer mixture. Approximately 4 mg of the pulverized mixture was weighed into an aluminum pan for DSC, and was kept at around 180 °C in the cell of a DSC (DSC2920, TA Instruments) for approximately 2 min under dry nitrogen gas flow (30 ml/min). The melted sample was transferred to a desiccator containing phosphorus pentoxide, and the desiccator was stored at a constant temperature of 30–70 °C. For the pure NTR enantiomer, the resolved enantiomer crystal (4 mg) was melt-quenched as described above to obtain an amorphous sample.

After certain periods of time, the change in heat capacity (ΔC_p) at T_g was measured for the stored amorphous samples by DSC at a heating rate of 20 °C/min. The amount of amorphous drug remaining in the sample at time t, $x(t)$, was calculated according to Eq. (1):

$$x(t) = \frac{\Delta C_{pt}}{\Delta C_{p0}} \quad (1)$$

where ΔC_{pt} and ΔC_{p0} are the ΔC_p values at time t and initially, respectively. The time required for 10% of the amorphous NTR to crystallize (t_{90}) was estimated as an indicator of the crystallization tendency. The time-profiles of $x(t)$ were analyzed according to the Avrami equation (Eq. (2), $n = 3$) to calculate t_{90}:

$$x(t) = \exp[-kt^n] \quad (2)$$

where k is the crystallization rate constant and n is the Avrami index. HPLC analysis of stored NTR samples showed no evidence of degradation during melt-quenching and subsequent storage.

2.3. Determination of nucleation rate and crystal growth rate of NTR enantiomer

The nucleation rate and the crystal growth rate were determined for samples prepared in a space between two glass disks separated by a stainless steel ring. The NTR enantiomer–polymer mixture, which was described above, or the crystalline NTR enantiomer (1.5–2 mg) was placed on a clean glass disk (thickness: 0.12 mm, diameter: 16 mm) and heated at 180 °C in the DSC with a stainless steel ring (inner diameter: 6 mm, thickness: 20 μm) as a spacer. After the sample had melted completely, it was covered with another glass disk (thickness: 0.12 mm, diameter: 12 mm) to yield an amorphous layer between the glasses. Attention was paid to ensure that the layer was free of bubbles. For measurements at temperatures above 40 °C, the sample was stored in the chamber of a heating/cooling stage for microscopy (THMS600, Linkam Scientific Instruments), which had been adjusted to a prescribed temperature in advance. The moisture in the chamber was removed by purging with dry nitrogen gas for 10–15 min. Microscopic images of the sample were recorded at appropriate time intervals by a digital camera (DXM1200F, Nikon Corporation) attached to a polarized light microscope (ECLIPSE E600 POL, Nikon Corporation) with a 10× objective lens. In order to minimize possible photo degradation of NTR by the polarized light, the light source of the microscope was shut off when images were not recorded. For measurements at 30 °C, the samples were stored at 30 °C in desiccators containing phosphorous pentoxide. After an appropriate period of storage, microscopic images of the sample were recorded, and the sample was again stored at 30 °C in a dry state.

2.3.1. Measurement of nucleation rate

The nucleation rate of the NTR enantiomers was estimated from time-profiles of nucleation site density determined from microscopic images of the stored samples. Nucleation site density per unit volume was calculated from the number of nucleation sites per unit area and the depth of field of the lens used for data collection. The depth of field was calculated to be 8.46 μm from the wavelength of the light (546 nm) and the numerical aperture of the lens (0.25). For samples with more than a dozen nucleation sites per fixed field at the end of the observation period, nucleation sites were counted in one fixed field. For samples with less than a dozen nucleation sites per field near the end of the observation period, and those stored at 30 °C, nucleation sites were counted for 12 individual areas in one sample, and the average value from the 12 individual images was regarded as the number of nucleation sites per field. The nucleation rate was obtained from the slope of time-profiles of the number of nucleation sites per unit volume (nucleation site density) at steady state. In cases showing preferential nucleation and growth at the sample periphery, these sites were not included in the analysis. The reported nucleation rates were average values of those obtained for at least three samples prepared separately.

2.3.2. Measurement of crystal growth rate

The crystal growth rates at temperatures above 40 °C were measured concurrently with the nucleation rate measurements as described above. The measurements at 30 °C were carried out using samples that showed more than a dozen nucleation sites per one field after a few months of storage in desiccators containing phosphorous pentoxide. The sample was placed in the chamber of the heating/cooling stage controlled at 30 °C, and the growth of crystals was observed in a fixed field. The radius of each crystal was estimated from a circular approximation by using Lumina Vision software (Mitani Co.). The average crystal growth rate was calculated from the increase in the radius as a function of time based on observations of at least 20 crystals.

2.4. FT-IR

FI-IR spectra were collected using a FT/IR-6300 (JASCO Corporation) by the KBr method at ambient room temperature. Transmission spectra were obtained for KBr disks containing 1–1.5% sample at a resolution of 0.4 cm^{-1} within the range of 4000–400 cm^{-1}. An accumulation of 128–256 scans was acquired for each disk.

3. Results

3.1. Effects of polymers on the overall crystallization rates of NTR enantiomers in solid dispersions

No significant differences in the melting point (158 °C), T_g (33 °C) and ΔC_p at T_g (0.40 J/g/K) were observed between (−)-NTR and (+)-NTR. Table 1 shows the T_g values of amorphous solid dispersions of (−)-NTR and (+)-NTR. There appeared to be no significant difference in the T_g values between the two. The solid dispersions containing HPMC (10–20%) and 5% PVP showed T_g values similar to that of each NTR enantiomer alone. T_g values for solid dispersions containing 10% PVP were slightly higher than that of each NTR enantiomer alone, whereas solid dispersions containing HPMCP (10–20%) exhibited T_g values slightly lower than that of each NTR enantiomer alone.

Fig. 2 shows time-profiles of overall crystallization of NTR enantiomers at 60 °C. No significant differences in the overall crystallization profiles were observed between (−)-NTR and (+)-NTR without polymer (Fig. 2(a)), and between (−)-NTR and (+)-NTR in solid dispersions containing 10% PVP (Fig. 2(b)). In contrast, differences in time-profiles between the enantiomers were observed for solid dispersions containing 10% HPMC or HPMCP: (+)-NTR crystallized more slowly than (−)-NTR, as shown in Fig. 2(c) and (d). Table 2 shows the t_{90} values for the amorphous NTR enantiomers obtained for NTR alone and NTR in the solid dispersions. The t_{90} values for (−)-NTR without polymer and those of solid dispersions containing 5–10% PVP were almost the same as the t_{90} values for (+)-NTR without polymer and those of solid dispersions containing 5–10% PVP, respectively, at the temperatures studied. The t_{90} values at 50 and 60 °C for (+)-NTR were 1.5–2.0 times longer than that for (−)-NTR in solid dispersions containing 10–20% HPMC or HPMCP. At 40 °C, however, any difference between the enantiomers was not clear.

Table 1
T_g of pure NTR enantiomers and their solid dispersions with a polymer.

Polymer	Polymer content [%]	T_g[a] [°C]	
		(−)-NTR	(+)-NTR
None	0	33.2 ± 0.1	33.1 ± 0.2
HPMC	10	33.1 ± 1.0	33.0 ± 0.7
	20	33.1 ± 0.8	33.0 ± 0.7
HPMCP	10	31.2 ± 0.7	31.0 ± 0.4
	20	30.8 ± 1.2	30.5 ± 0.9
PVP	5	33.0 ± 0.2	33.1 ± 0.2
	10	36.3 ± 1.2	36.2 ± 0.8

[a] Average ± standard deviation (n = 3).

3.2. Effects of polymers on the nucleation rate and crystal growth rate

Fig. 3 shows the typical micrographs of NTR crystals grown from amorphous pure enantiomers and their solid dispersions with a polymer. The recrystallized NTR enantiomers without polymers showed a melting point of 158 °C, suggesting the same crystal form as the originally resolved stable one. The melting point of the samples containing 10% HPMC, HPMCP and PVP was approximately 151 °C in all cases, regardless of the various crystal shapes shown in Fig. 3. The difference from the melting point of the pure enantiomers would have been due to melting point depression by the

Table 2
t_{90} for NTR enantiomers with and without polymer.

Temperature [°C]	Polymer	[%]	t_{90}[a] [h]			
			(−)-NTR		(+)-NTR	
40	None	0	41	(1)	41	(1)
	HPMC	10	230, 240[b]		230, 230[b]	
	HPMCP	10	49	(1)	49	(1)
50	None	0	5.7	(0.2)	5.7	(0.1)
	PVP	10	250	(10)	240	(4)
	HPMC	10	17	(0.4)	25	(0.1)
	HPMCP	10	6.1	(0.3)	11	(0.3)
60	None	0	1.1	(0.1)	1.1	(0.1)
	PVP	5	3.5	(0.1)	3.6	(0.1)
		10	25 ± 3[c]		25 ± 3[c]	
	HPMC	10	3.8, 4.1[b]		6.7, 6.9[b]	
		20	8.7	(0.3)	15	(0.4)
	HPMCP	10	1.5 ± 0.2[c]		2.7 ± 0.3[c]	
		20	3.2	(0.1)	6.4	(0.2)

[a] The values in parentheses are standard error estimated from single experiments using Origin 8.1 software (Lightstone Corp.).
[b] Results with two values represent the results obtained from duplicate experiments using separately prepared samples.
[c] Mean ± standard deviation (n = 3).

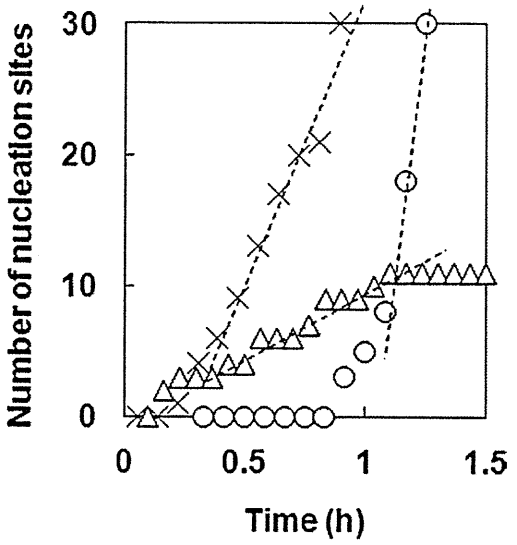

Fig. 4. Time profiles of the number of nucleation sites per field of view for (+)-NTR at 50 °C (○), 60 °C (×) and 70 °C (△). The dotted lines show the linear regression at steady state.

added polymers, as the melting point fell gradually with increasing polymer content (data not shown). The data suggested that differences in crystal habit, rather than polymorphism, might have been responsible for the differences in crystal shape among the solid dispersions.

Fig. 4 shows the typical time-profiles of the nucleation of amorphous NTR enantiomer stored at various temperatures. The lower the storage temperature, the longer the period required before the first crystal was observed. The nucleation rates at steady state were obtained from the slope of the lines in Fig. 4, and these were plotted against storage temperature (Fig. 5). As expected from the similar overall crystallization profiles of the NTR enantiomers (Fig. 2(a) and (b)), no significant difference in the nucleation rates between (−)-NTR and (+)-NTR was observed for amorphous NTR alone and the solid dispersions containing PVP within the temperature range studied (Fig. 5(a)). In contrast, the nucleation rates of (+)-NTR were lower than those of (−)-NTR in the solid dispersions containing HPMC and HPMCP (Fig. 5(b)) within the temperature range of 50–70 °C. At 40 °C, however, the differences in the rates between (−)-NTR and (+)-NTR were not pronounced. These results were consistent with the t_{90} values of the enantiomers shown in Table 2.

Fig. 6 shows the typical time-profiles of the NTR crystal growth at 60 °C. Crystal radius increased linearly with time, and the growth rate was estimated from linear regression of the plots. The higher the temperature, the faster the crystals grew within the temperature range studied (Fig. 7). In contrast to the nucleation rates, no significant growth rate differences between the NTR enantiomers were observed, irrespective of the absence or presence of any polymer.

3.3. FT-IR

FT-IR spectra (4000–400 cm^{-1}) of (−)-NTR and (+)-NTR were indistinguishable from one another for both the amorphous and the crystalline forms. Similarly, the FT-IR spectra of amorphous solid dispersions were almost the same for (−)-NTR and (+)-NTR with any polymer. Fig. 8 shows the spectra for crystalline (−)-NTR (dotted line in Fig. 8 (a)), NTR solid dispersions containing 25–75% HPMC and HPMC alone (dotted line in Fig. 8 (c)) in the range of 1800–1550 cm^{-1}, corresponding to C=O stretching region of NTR. Spectra with and without an asterisk represent that of (−)-NTR

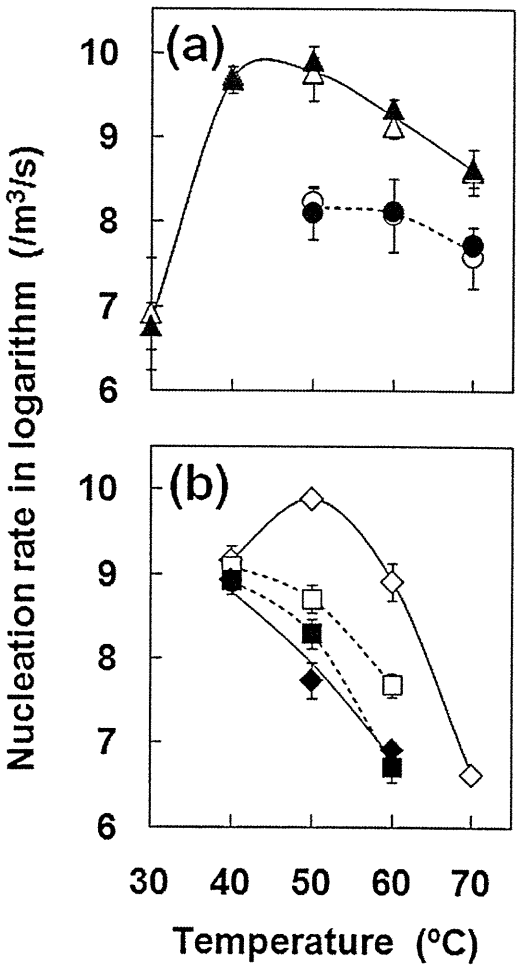

Fig. 5. Plots of nucleation rate as a function of temperature. Error bars represent standard deviation for at least triplicate experiments. (a) △, ▲: without polymer, ○, ●: 10% PVP and (b) □, ■: 10% HPMC, ◇, ♦: 10% HPMCP. Open symbols represent (−)-NTR and solid symbols represent (+)-NTR.

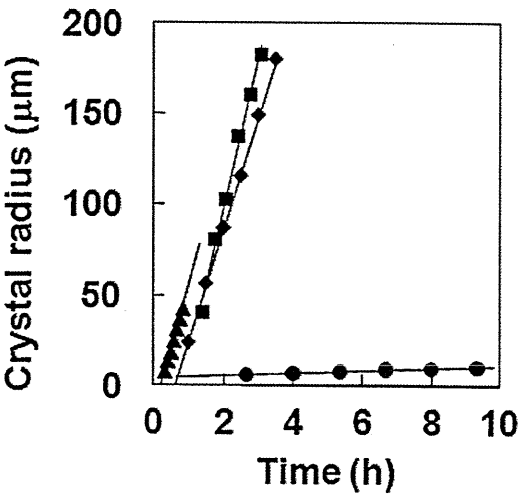

Fig. 6. Typical time profiles of the radius of NTR crystals in (+)-NTR alone (▲), and solid dispersions with 10% HPMC (■), 10% HPMCP (♦) and 10% PVP (●) at 60 °C.